Adaptive Optics for High Resolution Imaging

Authors:
Karen M Hampson[1], Raphaël Turcotte[1,2], Donald Miller[3], Kazuhiro Kurokawa[3], Jared R Males[4], Na Ji[5] and Martin J Booth[1*]
[1] *Department of Engineering Science, University of Oxford, Oxford OX1 3PJ, UK*
[2] *Tech4Health Institute, NYU Langone Health, New York, NY 10010, USA*
[3] *School of Optometry, Indiana University, Bloomington, Indiana 47405, USA*
[4] *Steward Observatory, University of Arizona, Tucson, AZ 85719, USA*
[5] *Department of Physics, Department of Molecular & Cellular Biology, University of California, Berkeley, USA*

*Corresponding Authors

Author contributions
Introduction (M.J.B., K.M.H., R.T.); Experimentation (M.J.B., K.M.H., R.T.); Results (M.J.B., D.M., K.K., J.R.M., N.J.); Applications (M.J.B., D.M., K.K., J.R.M., N.J.); Reproducibility and data deposition (M.J.B., R.T., D.M., K.K., J.R.M., N.J.); Limitations and optimizations (M.J.B., D.M., K.K., J.R.M., N.J.); Outlook (M.J.B., K.M.H., R.T.); Overview of the Primer (M.J.B.).

Abstract:

Adaptive optics (AO), a technique that corrects for optical aberrations, was originally proposed to correct for the blurring effect of atmospheric turbulence on images in ground-based telescopes; indeed, the technique was instrumental in the work that resulted in the discovery of a supermassive compact object at the centre of our galaxy, which was awarded the 2020 Nobel Prize in physics. When AO is used to correct for the eye's imperfect optics, retinal changes at the cellular level can be detected, allowing us to study the operation of the visual system and to assess ocular health in the microscopic domain. By correcting for sample-induced blur in microscopy, it has pushed the boundaries of imaging in thick tissue specimens, such as when observing neuronal processes in the brain. The focus of this primer is the application of AO for high resolution imaging in astronomy, vision science, and microscopy. It begins with an overview of the general principles of AO and its main components, which include methods to measure the aberrations and devices for their correction. These components are linked in operation via a control system. Results and applications from each field are presented, along with reproducibility considerations and limitations. Finally, future directions are discussed.

[H1] Introduction

High resolution optical imaging relies upon the high fidelity focussing of light. Light can be described in terms of optical fields **[G]**, and thus its properties are parametrized for a given wavelength at each point in space and time in terms of amplitude, phase and polarization. However, these fields can be perturbed (in amplitude, phase and polarization) as they propagate through optical systems and other media, and the performance of the imaging systems can be highly sensitive to those perturbations. For instance, astronomical image quality is limited by atmospheric turbulence; microscopes produce blurred images when samples have a non-uniform refractive index distribution; and ophthalmoscopes that image the back of the eye are detrimentally affected by the eye's imperfect optics. Adaptive optics (AO) is an ensemble of electro-optical and computational methods that aim at recovering the optimal performance of an optical system[1–6]. This has brought benefits to a range of applications. For example, by integrating AO in their telescopes, astronomers have been able to expand the observation of celestial bodies[7]. Implemented into microscopes, AO has enabled neuroscientists to monitor the activity of neurons embedded deep inside the living mammalian brain[8,9]. And integrated into ophthalmoscopes, vision scientists and ophthalmologists are able to visualize, quantify, and track *in situ* the many different types of cells that compose the retina, offering significant clinical potential[10–14].

There are many imaging applications in which AO has a significant impact, and the above list is far from exhaustive. Compensation **[G]** through modulation of the optical field is the fundamental working principle through which AO alleviates the effect of optical aberrations[15]. Most commonly, we consider aberrations as variations in phase of the optical field. Such phase variations are equivalent to changes in the wavefront shape[16]. In general, aberrations can thus be understood as deformations of the light's wavefront from its perfect form – planar for a collimated beam or spherical for a focussed beam – that produces the sharpest image[1,2]. Wavefront aberrations, such as those caused by refractive index variations in biological tissue or air motion, can be rectified by locally modulating the phase of the light such that the effects of the aberrations and the applied modulation cancel out[16]. In other words, the optimal wavefront shape is recovered by introducing a modulated wavefront with phase conjugate to the problematic aberration. This process of correction is one of the two essential components shared by all AO methods. The other process consists of evaluating (sensing) the aberrations, in order to determine the optimal phase compensation. Rather than using a dedicated sensor, the image can also be used to determine the appropriate correction. There is wide diversity in approaches to realise both sensing and correction[1–4]. In addition, implementation requirements can vary widely amongst fields in which AO is used; hence, translating key concepts and methods across applications is challenging. However, connecting these concepts is worthwhile, as fundamental advances in AO originate from all these application areas and developers can benefit from important advances in separate fields.

In this Primer, we aim to provide a unified perspective on AO for imaging applications by highlighting commonalities, and differences where necessary, in experimentation amongst fields. We present results from astronomy, vision science and microscopy to illustrate the potential of AO for improving images in a range of imaging modalities and then discuss how these improvements afforded by AO facilitate, and even enable, new scientific discoveries in diverse applications. For this purpose, exemplar results and applications were selected and are discussed to varying levels of details to reflect intrinsic properties of AO in the different fields and modalities. Information about external resources is given to ease the adoption of AO and support reproducibility. Finally, current limitations of AO methods are considered before we present an outlook on anticipated technology development.

[H1] Experimentation

Different application fields using AO for imaging have their particular technical requirements and AO implementations. However, there are many underpinning concepts that are common to all applications. In this section, we review the fundamental principles and methods of implementing AO and how and why this varies for different fields.

[H2] Generic AO System for Imaging

The image quality of an optical system is typically characterized by its point spread function (PSF). The PSF characterizes how the image of a point is blurred when light passes through the optical system. The degree of blurring depends upon the shape of the wavefront. Figure 1a illustrates the concept of a wavefront and its distortion. The propagation of light represented conceptually by multiple adjacent waves. The shape of the wavefront, *W*, is found by joining up the peaks of each wave, i.e. where the light has the same phase. Note that the ray directions are locally orthogonal to the wavefront. Initially the wavefront is planar. When the light reaches an object having a non-uniform refractive index distribution, the different waves travel at different speeds, causing them to be delayed with respect to each other. In the example shown the central wave travels through a relatively higher refractive index, which causes the light in that region to travel more slowly. The consequence of this is that the outgoing waves are now out of phase owing to the difference in optical path length **[G]**. The PSF of an imaging system depends on the shape of the wavefront in the so-called pupil plane of the system, where the limiting optical aperture is typically placed. While the above example is two-dimensional for simplicity, it should be kept in mind that a wavefront is a surface in a three-dimensional space. For an aberration-free system, the wavefront is planar in the pupil plane, as the light is typically collimated **[G]**. This results in a spherical wave when the light is focussed **[G]** to form the image. The resulting PSF is diffraction-limited **[G]**, as shown in Figure 1b. This is the smallest obtainable image of a point and sets the resolution limit of an imaging system (unless super-resolution techniques are employed, such as structured illumination)[17]. According to the Rayleigh resolution criterion, in order for two point objects to be resolved, the maximum intensity of one object must lie on the first minimum of the PSF of the other. The narrower the PSF, the closer the two objects can be in order to be resolved. This resolution, *R*, is set by the diffraction limit and given by

$$R = \frac{1.22\lambda f}{d} \quad (1)$$

where λ is the wavelength, *f* is the focal length **[G]**, and *d* is the pupil diameter.

When aberrations are present, for example owing to refractive index inhomogeneities in the medium through which the light must pass, as in the case of microscopy and astronomy, or the optical components essentially having a non-ideal shape, as in the case for vision science, the wavefront is no longer described by a plane or spherical wave, as shown in Figure 1c. Consequently, the maximum intensity of the PSF is reduced and the width of the PSF is increased, resulting in reduced image resolution and contrast, as shown by comparing the right-hand side of Figures 1b and 1c. The goal of AO is to introduce a distortion that is equal in magnitude, but opposite in sign to that of the aberrated wavefront, in order to correct for aberrations and achieve diffraction-limited image quality with maximal signal. This is achieved by changing the optical path length using deformable mirrors, for example. The magnitude of the wavefront distortion is typically specified in micrometres (μm). To achieve diffraction-limited resolution, i.e. a Strehl ratio **[G]** of 0.8 or above, AO must reduce this distortion to less than λ/14. Note that amplitude variations, where the amplitude is denoted by the peak to valley of the wave as shown in Figure 1a and manifest as intensity variation, are typically neglected. This is primarily due to phase distortions having a more pronounced effect on the imaging properties. Also, with current devices, intensity correction would involve introducing losses. Similarly, distortions of the polarization state are also often neglected, although polarization control is gaining interest in microscopy, as it is important in some imaging modalities[18,19].

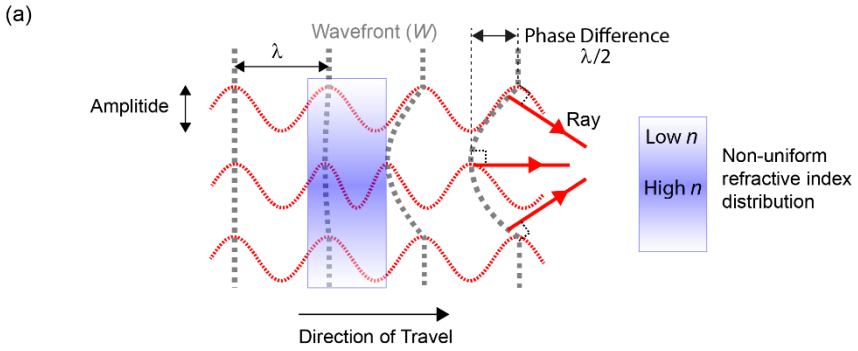
(a)
Wavefront (W)
λ
Phase Difference
λ/2
Amplitide
Ray
Low n
High n
Non-uniform
refractive index
distribution
Direction of Travel

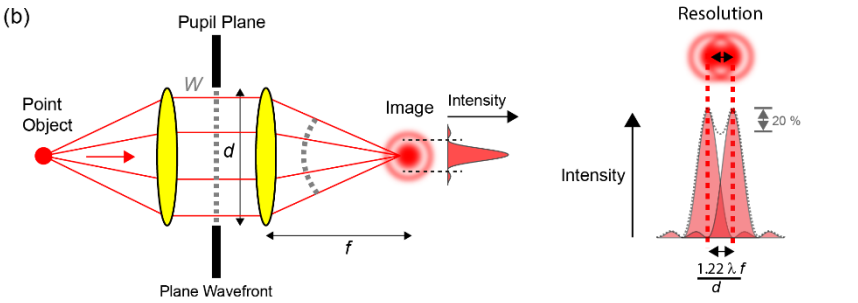
(b)
Pupil Plane
W
Point
Object
d
Image
Intensity
f
Plane Wavefront
Resolution
Intensity
20 %
1.22 λ f
d

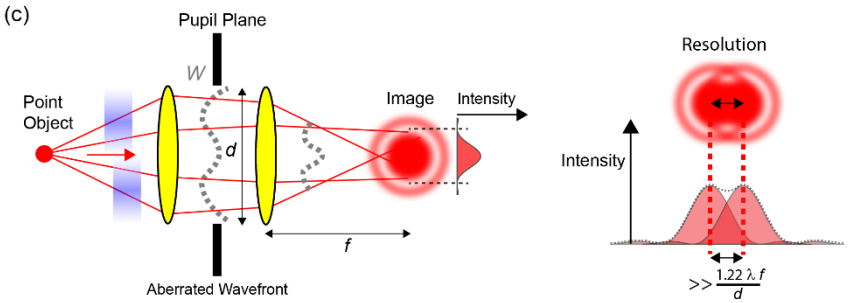
(c)
Pupil Plane
W
Point
Object
d
Image
Intensity
f
Aberrated Wavefront
Resolution
Intensity
>> 1.22 λ f
d

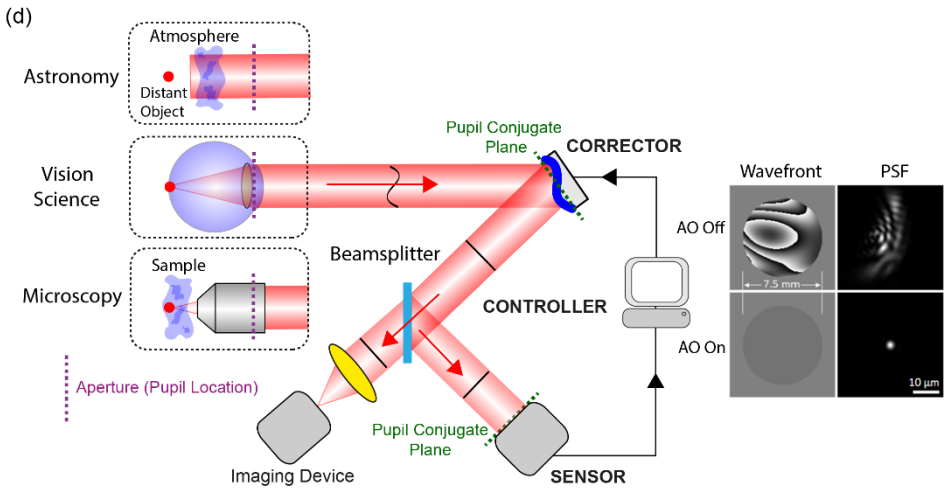
(d)
Atmosphere
Astronomy
Distant
Object
Vision
Science
Sample
Microscopy
Aperture (Pupil Location)
Pupil Conjugate
Plane
CORRECTOR
Beamsplitter
CONTROLLER
Pupil Conjugate
Plane
Imaging Device
SENSOR
Wavefront
PSF
AO Off
AO On
7.5 mm
10 µm

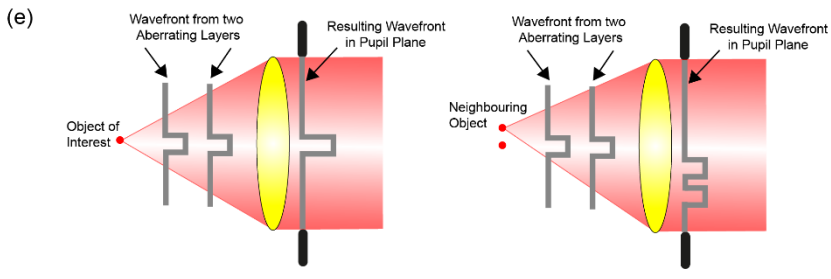
(e)
Wavefront from two
Aberrating Layers
Resulting Wavefront
in Pupil Plane
Object of
Interest
Wavefront from two
Aberrating Layers
Resulting Wavefront
in Pupil Plane
Neighbouring
Object

Figure 1. (a) Relationship between the wavefront and how it is affected by changes in optical path. The central light wave is slowed down relative to the outer light waves owing to it passing through a higher refractive index. The result is the wavefront becoming distorted. (b) In an aberration-free system, the wavefront is planar in the pupil plane and resolution is diffraction-limited. (c) When aberrations are present, the pupil-plane wavefront is distorted, and resolution is decreased. The grey dashed lines represent the normalised sum of the individual PSFs. (d) General AO system. The corrector shown here is a deformable mirror, but could in principle be another device. Wavefront aberrations at the eye's pupil and corresponding PSFs at the retina for a typical eye with and without perfect AO. Wavefront maps are shown with a modulo-2π grayscale. (e) How multiple aberration layers affect the pupil wavefront for different points in the imaged field.

A general AO imaging system is shown in Figure 1d. It consists of three main components: a sensor to measure the aberrations; a corrector to compensate the aberrations; and a controller that calculates the required signals sent to the corrector, based on the sensor measurements. The corrector and sensor are typically conjugate to the pupil plane (aperture stop location) of the imaging system, which means that the pupil is imaged on to the corrector and sensor. In the case of microscopy, the pupil is the aperture of the objective lens that transfers light to and from the specimen. For vision science, it is the eye's pupil and for astronomy, it is the telescope aperture. Conjugation of the corrector, sensor, and system pupil is achieved via pairs of lenses or curved mirrors (relay telescopes) that reimage each one on to the next[20–22]. AO systems are typically designed using commercial optical ray tracing software (e.g., Zemax, LLC, WA), constructed from a myriad of mostly high-end stock lenses and mirrors. In some AO systems, there is no dedicated wavefront sensor and the quality of the image is used to control the corrector. While this has some advantages, such as reduced system complexity, it is not suitable for situations in which the aberrations are rapidly evolving, as it can be slow. Consequently, this technique is mainly confined to microscopy. This will be discussed further in section 2.3. Note that the system shown in Figure 1d is for a generic imaging system. Different fields have a variety of different imaging systems with specific AO implementation.

Across all fields, the aberrations that are induced, originate from multiple layers. In astronomy the turbulence varies with altitude, while in the eye aberrations are introduced mostly by the surfaces of the crystalline lens and cornea. For microscopy, there can be a volume of inhomogeneous tissue in front of the object of interest. This means that the shape of the wavefront varies depending upon the location of the object of interest is as shown in Figure 1e. The most straight forward method is to update a single corrector accordingly. Use of a single corrector is referred to single conjugate AO and is the most widely used implementation of AO. A less commonly employed method is to use multiple correctors, in which each corrector is conjugates to a different layer or depth. This is referred to multiconjugate AO[23–25]. This adds significant cost and complexity to an AO system.

The area over which the aberrations can be considered invariant is referred to as the isoplanatic patch. Typical values for the isoplanatic patch for astronomy are 1.5" to 2" at a wavelength of 0.5 um varying with seeing and turbulence layer heights, and it scales with wavelength to the 6/5 power[3,26]. For vision science it is approximately 1°, or 300 µm at the retina[27]. In the case of microscopy, the patch size ranges from hundreds of microns, in mouse brain for example[8,28,29], to a few microns, such as inside tissue with high curvature or complexity, for example zebrafish larvae[30] and C. Elegans[29,31]. Although a single corrector is commonly placed in a pupil conjugate plane, it can be more advantageous to place a single corrector conjugate to the layer introducing the most significant aberrations. This can widen the field of view over which sharp images are obtained. This is referred to as ground-layer AO in astronomy and sample-conjugate AO in microscopy[32].

In all cases, temporal dynamics of the perturbations must be taken into consideration as this has implications for the way in which adaptive optics is implemented. While some perturbations are relatively stable, such as is often the case in many microscopy applications, those due to dynamic processes in the eye can vary significantly, with those due to atmospheric turbulence evolving even faster. We note that in astronomy there is a distinction between active and adaptive optics. Active optics is much slower and involves changing the shape of the telescope mirrors to account for environmental factors and to align and collimate the telescope, not correct aberrations due to turbulence. There is no such semantic distinction in vision science and microscopy.

[H2] Aberration Characteristics

When implementing AO, it is important to consider the properties of the aberrations that are to be corrected. This includes what type of aberrations are present, and how rapidly the wavefront changes shape over time. The shape of the wavefront, *W*, can be considered to consist of a sum of shapes, or modes. It is common for these modes to be expressed in terms of Zernike polynomials[33]:

$$W(\rho,\theta) = \sum_{n=0}^{\infty} \sum_{m=-n}^{n} a_n^m Z_n^m(\rho,\theta), \quad (2)$$

where ρ is the normalised pupil radius ranging from zero to one, Θ is the angle around the optic axis, and a_n^m is the coefficient (or magnitude) of the Zernike polynomial $Z_n^m(\rho,\theta)$ with the azimuthal frequency *m* and radial order *n*. We note that there

are certain constraints on the allowable values of *m* and *n*. Each polynomial describes the shape of the wavefront for a given aberration. Each of these modes are shown in Figure 2. Several Zernike modes correspond closely to aberrations used in classical optics such as astigmatism and coma for example. An advantage of Zernike polynomials are that they are orthogonal, i.e. they have convenient mathematical properties that permit us to consider them as having independent effects on the optical system. There are slight variations on the definition of Zernike polynomials, such as whether the angles are measured clockwise or anticlockwise, for example. Figure 2 shows the Zernike aberrations, as defined by the Noll convention **[G]**[34], which are typically used in astronomy and microscopy. The OSA ANSI is commonly used in vision science[35]. One of the reasons that this convention is used in this case is because the way in in which the angle is measured matches the way it is defined when determining a patient's spectacle or contact lens prescription. The piston mode (which is a constant phase offset) is not considered when correcting the wavefront as it does not affect the image because it merely represents translation of the wavefront along the optical axis. Tip and tilt represent a shift in the position of the image and so are not usually corrected for in microscopy with stationary samples. In vision science, even when the eye is fixated on a static object, miniature eye movements cause the retina to rapidly move around. In scanning imaging systems for the eye, in which the image is built up line by line, this can cause image distortion. Tip and tilt changes due to atmospheric turbulence also cause image blur that needs to be corrected. Note that in the literature, aberration modes are often broadly categorised as being low order or higher order. The definition of lower order and higher order varies between fields. For astronomy higher order is typically defined as modes with a radial order above three, above two for vision science and above four for microscopy.

In astronomy and vision science, there are statistical models of the aberrations[36–38]. These mathematical models generate the sort of aberrations that are likely to occur. Consequently, the aberration statistical properties can be determined based on experimental parameters such as pupil diameter of the eye or the telescope[39]. In astronomy, the number of Zernike modes corrected varies from facility to facility and depends on the type of AO implementation, but can vary from on the order of one hundred to several thousand, i.e. radial orders from 15 to ~70. The higher the radial order the lower the magnitude[34]. The peak-to-valley amplitude is typically 1-3 µm *rms* (root mean square)[34]. The dominant source of temporal evolution is wind-driven motion of the atmosphere[40]. Depending on telescope diameter and wind speed, aberrations can vary with frequencies up to 100 Hz[41]. The variation in aberration magnitude with temporal frequency follows a power law with an exponent of -17/3[42,43]. In vision science, the aberrations increase with pupil size and typically the higher the Zernike radial order, the smaller the magnitude of the aberration[44]. A large pupil is often used for imaging the retina to increase resolution. For a 7.5 mm pupil, to achieve diffraction-limited imaging in 95% of the population requires correcting the Zernike radial orders from two to nine[38]. The peak-to-valley of the wavefront is around 11 µm. This value is much higher if they require a spectacle prescription (radial order two). These aberrations also temporally vary, due to factors most likely related to dynamics in the optics of the eye, such as due to the heartbeat, tear film, and movement of the eye. The power law exponent of these fluctuations is about -1.3[45,46]. Today's ophthalmic AO systems are generally designed to handle dynamic aberrations up to a couple of Hertz, but a recent study that included many more subjects suggests that correcting fluctuations varying at higher frequencies may be necessary to achieve diffraction limited performance in most eyes[47].

Although the aberration characteristics of some microscopy samples have been shown to be similar to that of astronomy with regards to the decrease in magnitude of the Zernike aberrations with increasing radial order[48], there are no comprehensive statistical models for microscopy, due to the vast range of specimen types for which AO might be used. Aberrations of samples with flat geometries and homogenous refractive index distributions are dominated by Zernike modes up to and including 4th radial order, while samples with more complex shaped surfaces and/or heterogeneous refractive index distributions require correction of many aberration modes beyond these. Similarly, the magnitudes of aberrations in microscopy depend on the sample, and can vary between sub-micrometer to several microns. Even for microscopy of live specimens, sample-induced aberrations usually do not rapidly vary over time. Therefore, AO measurement and correction do not have to be carried out at high speed.

A useful descriptor to capture the severity of the aberrations in a system is the root mean square (rms) wavefront error. This is given by the square root of the sum of the squared coefficients. The aim of AO is to reduce this value to less than $\lambda/14$ in order to obtain diffraction-limited resolution. While Zernike modes are commonly used, they are not the only – nor necessarily the best – representation used for a particular application. Other analytically or empirically defined modes sets can also be used that represent a more efficient basis than Zernike modes. For vision science for example see[38,49]. Furthermore, when operating an AO system, it is often convenient to think of the wavefront as consisting of discrete non-overlapping zones (segments), as opposed to a sum of superimposed modes. The choice of modes or zones often depends on the implementation of sensing and correction, which is discussed further in the relevant sections.

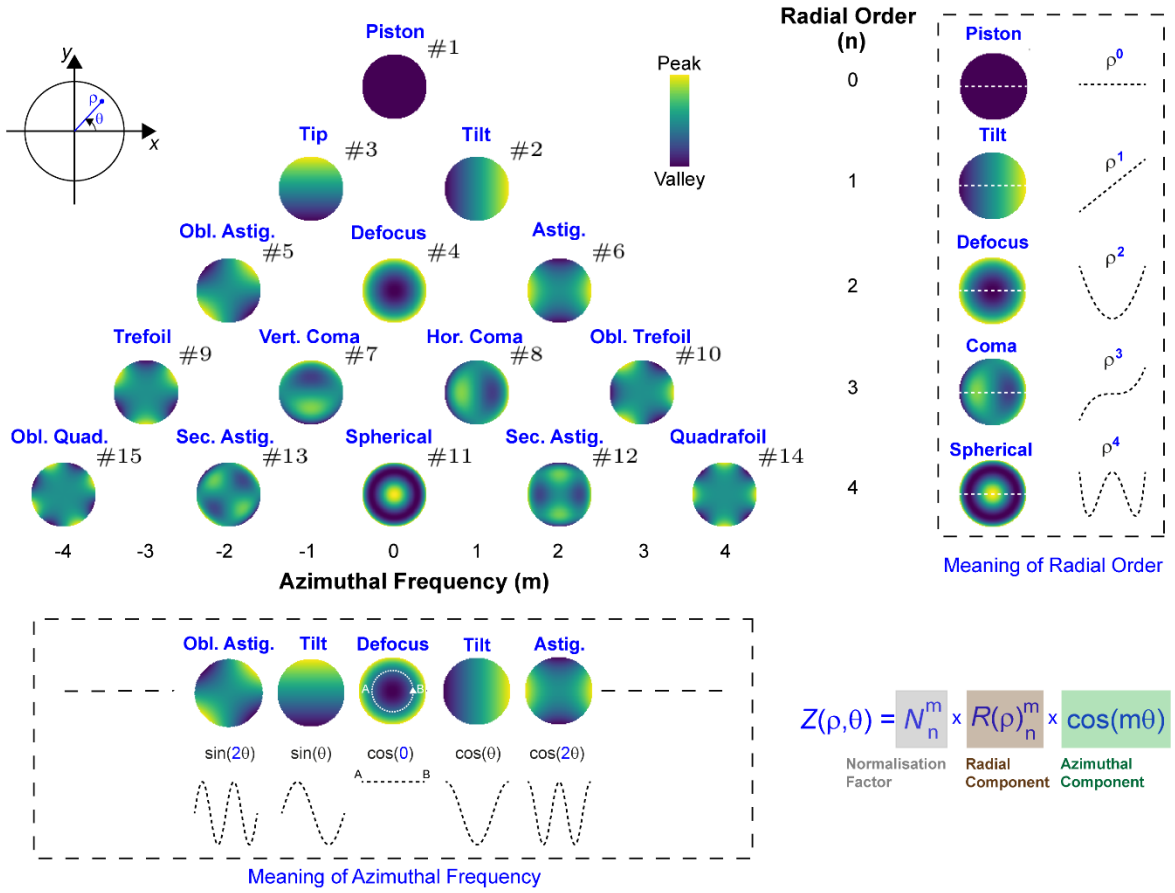

Figure 2. Modal representation of aberrations using Zernike polynomials according to the Noll notation[34]. Figure from[50]. The polynomials are organised according to their radial order *n* and azimuthal frequency *m*. The radial component describes how the polynomial varies with the radius, *ρ*. For example, a mode with a radial order two means that the polynomial describing the mode has a mathematical term where the highest power is two, i.e. it has a leading ρ^2 term. The azimuthal frequency describes how the polynomial varies with angle, θ. The positive numbers represent a cosinusoidal variation, with negative numbers representing sinusoidal variation. A value of 2 means that the polynomial varies with cos(2θ), for example.

[H2] Aberration Measurement

Aberrations can be measured most directly using a dedicated wavefront sensor, or they can be determined indirectly from the images. We will refer to these two methods as direct sensing and indirect sensing, respectively. The indirect method is often referred to as sensorless AO as there is no dedicated wavefront sensor. Indirect methods are significantly slower than sensor-based methods at determining the magnitude of the aberrations present, and hence the required correction. This is because they typically require collecting many images. Depending on the imaging speed, indirect methods can take seconds to minutes to determine the required correction in comparison to milliseconds for a dedicated wavefront sensor. As the aberrations in microscopy are mostly static, indirect methods are more suited to this field. They have been used to some extent in vision science, see for example[51], owing to the advantage of requiring no extra sensing hardware. However, for astronomy, where the aberrations due to atmospheric turbulence evolve at high rates, the slow speed of indirect sensing would present a significant problem[41].

[H3] Direct Sensing

The most widely used sensor to measure the aberrations across all fields in an AO system is the Shack-Hartmann (SH) sensor, as it can be quick, simple and effective[16]. The principle of operation is shown in Figure 3a. It consists of an array of lenslets **[G]** placed in a conjugate pupil plane and a camera at the focal plane of the lenslets[52]. For an aberration-free (i.e. perfect) wavefront, a regular (i.e. evenly spaced) array of spots is formed on the camera. For an aberrated wavefront, the location of each spot is shifted according to the local tilt (slope) of the wavefront across that given lenslet as shown in Figure 3b. Typically, a minimum of four camera pixels per spot is required to accurately determine its location. There are a variety of algorithms for determining the spot locations, with the centre-of-mass being one of the most frequently used[53]. Finding the centre of the spot using the centre-of-mass is often referred to as centroiding.

Note that the traditional implementation of the SH sensor requires light returning from a point source, to inform the sensor measurements. In microscopy, this could be light originating from a point object such as a fluorescent bead for example. In vision science the retina is typically illuminated with a point of light from an infrared light source. If the light informing the SH sensor is not confined axially and laterally the SH spots will become elongated. Figure 3c shows an example of spot elongation owing to an axially extended object where light is returning from multiple depths. This effect is more pronounced with higher numerical apertures and so can occur more so in microscopy than vision science[54,55]. In this case, an image conjugate aperture can be used to as shown in Figure 3c[56] or more advanced algorithms must be implemented[57]. Spot elongation is inherent in astronomy when using laser guide stars to provide light to inform the wavefront sensing measurements. Some astronomical AO systems implement image-based Shack-Hartmann wavefront sensing[57], in which the image of the object of interest, such as the surface of the sun, forms behind each lenslet, and the shift of each of these images determines the local slope of the wavefront. An advantage of this technique is that there is no need for an extra light source for the SH. This technique is starting to be adopted in microscopy[58] but has yet to be used in vision science. In astronomy, multiple wavefront sensors can be used to reconstruct the turbulence based on measurements from multiple guide stars, even if a single corrector (SCAO) is to be used. This is referred to as tomographic AO and is used to calculate the shape of the corrector for aberration-free imaging of an object of interest within the field of view. This is because the light from a single guide star can take a very different path through the turbulence in comparison to the light from the object. Consequently the aberration measurements from a single guide star may not be appropriate.

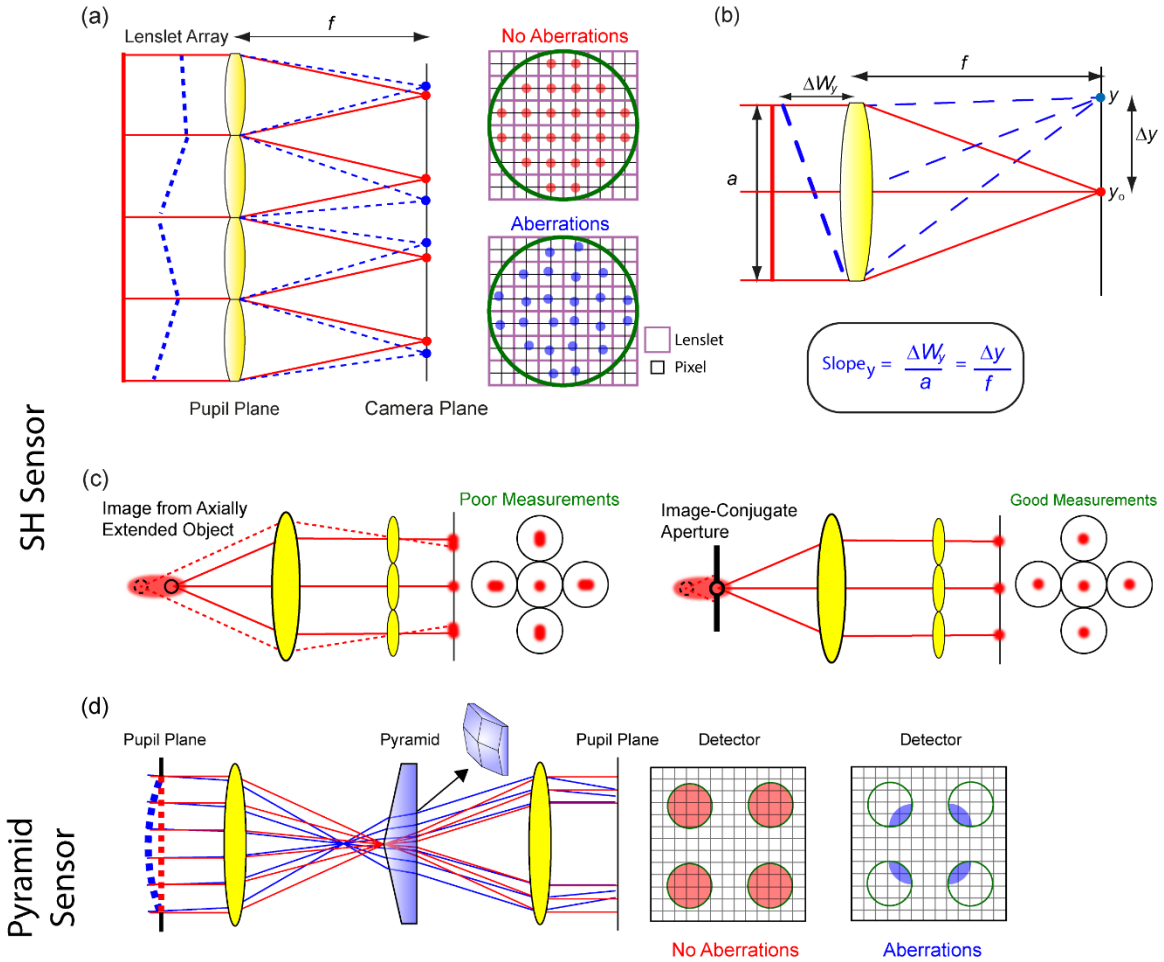

Figure 3. Principles of the Shack-Hartmann wavefront sensor and pyramid wavefront sensor. (a) The Shack-Hartmann sensor consists of a lenslet array conjugate to the pupil plane and a camera placed at the focal plane of the array. For an aberration-free wavefront, a regularly spaced array of spots is formed on the camera. In the example shown there are four camera pixels behind each lenslet. (b) Aberrations shift each spot according to the local wavefront slope, $slope_y$, across each lenslet. The magnitude of the wavefront, ΔW_y, across a lenslet of diameter a, is determined from the shift in the spot, Δy, divided by the focal length, f. (c) In order to obtain the slope using conventional SH algorithms, the light returning from the object must be point-like, i.e. confined axially and laterally. Otherwise, the Shack-Hartmann spots will be elongated, which can adversely affect the algorithm to determine their precise location. For light that is axially elongated, an image conjugate aperture can be used to alleviate these problems by reducing out-of-focus light. (d) Pyramid wavefront sensor. A four-faceted prism is placed at the focal plane and forms four images of the pupil. For an aberration-free (planar) wavefront, four pupil images, with identical intensity distributions, are imaged on to the detector. Aberrations result in changes to the intensity distribution of each pupil image. An example for defocus is shown.

When using a deformable mirror as the corrector, astronomical and microscopy AO systems typically use a ratio of the total number of lenslets to the total number of actuators (elements that deform the mirror) of around one, owing to limited light[9,16]. For ophthalmic AO systems, where considerably more light is available for wavefront sensing, a minimum ratio of about two has been reported optimal[59], but a typical ratio in actual systems is between three and six. Once the ratio has been set, the focal length should be chosen to be the longest possible before the SH spots cross in to regions behind neighbouring lenslets. This is to keep the highest sensitivity possible without exceeding the desired dynamic range **[G]**. The longer the focal length the higher the sensitivity in detecting the movement of the spots, but if the focal length is too large, the spots will quickly cross into regions behind neighbouring lenslets, thus reducing the dynamic range. Consequently, there is a trade-off between sensitivity and dynamic range.

While the SH is the most widely used sensor, there are several alternatives[16]. For instance, curvature sensors have been used in astronomy but are being phased out, while pyramid sensors are increasingly present. Figure 3d shows the principle of operation of the pyramid wavefront sensor, which uses a different principle to encode phase variations into intensity measurements[60]. The tip of a four-faceted prism is placed at the image plane and the prism forms four images of the pupil. The aberrations present are determined from the relative intensity distributions of the pupil images. For a plane (i.e. aberration-free) wavefront, each pupil image is illuminated identically. In the case of defocus being present for example, the light is refracted by the prism such that each pupil is illuminated differently. An advantage of this sensor is that the dynamic range and sensitivity can be adjusted independently in comparison to the SH[61]. This means that a wider range of aberration magnitudes, from low to high, can be measured accurately. This sensor has been demonstrated across fields[61–63] but is not yet used as extensively as the SH sensor, perhaps due to its introduction in the field of AO being later than the SH. In future there may be other direct-sensing alternatives to the SH sensor such as the use of diffusive plates, where the local wavefront slope is determined from the local shift in the resultant speckle pattern[64]. Another approach is to use machine learning to improve the sensor performance in heavy scattering, scintillation, or when sensor spots are distorted or obscured[64,65].

[H3] Indirect Sensing

Two main types of indirect sensing are modal and zonal. In the modal case, a continuous surface wavefront corrector is used, and the wavefront is considered to consist of the sum of aberration types, also referred to as modes, as illustrated in Figure 2. Individual aberration modes, such as Zernike modes, are applied sequentially to the wavefront corrector and changes in the image are quantified using an image quality metric, such as intensity or image sharpness[1]. Figure 4a shows a simple example in which coma is present. By applying different magnitudes of coma to the corrector and measuring the intensity in the image, a parabolic curve can be fit to the data points to determine the optimum amount of coma that must be introduced to obtain a clear image. Other modes can be corrected in similar way. Recent work has shown that wavelet **[G]** decomposition of images provides a versatile way to define optimisation metrics for indirect sensing[66]. There are a number of algorithms that have been used to determine the correction in modal schemes[5,67].

In the zonal case, rather than considering the wavefront as consisting of aberration modes across the whole pupil, it is considered as discrete non-overlapping zones. This method is often used with segmented correctors. Figure 4b shows an example of the pupil segmentation zonal method where the required tilt of each zone to correct the wavefront, by ensuring rays meet at the focus, is determined from shifts in the image. To ensure that the rays arriving at the focus are also in phase, piston (forwards-backwards position) of each segment is determined from intensity measurements with differing amounts of piston applied[68,69]. Note that some wavefront correctors, such as liquid crystal spatial light modulators (LCSLMs), can only perform piston modulation. In this case, rather than mirrored segments that move back and forth, the refractive index of their pixels is changed. To determine the required piston introduced by each mirrored segment or pixel, simultaneously, the piston for each can be modulated at a different frequency and the power spectrum components can be used[29]. Note that indirect sensing has also been used in vision science using a variety of different modal-based algorithms, see for example[51].

Phase retrieval and phase diversity are other methods for indirect wavefront sensing[70]. Phase retrieval is an iterative algorithm that evaluates the local wavefront curvature from the difference in intensity between images of a point source. The simplest implementation of phase retrieval consists of acquiring two images of a fluorescent bead with different but known values of defocus. This approach is commonly used in microscopy to correct for static aberrations introduced by the optical system[30,71]. Phase diversity operates on images of a spatially extended source and requires multiple phase masks at the pupil to calculate the local wavefront curvature from the difference in intensity between images. Phase diversity has been employed in astronomy to correct aberrations originating from the system (i.e. telescope)[72].

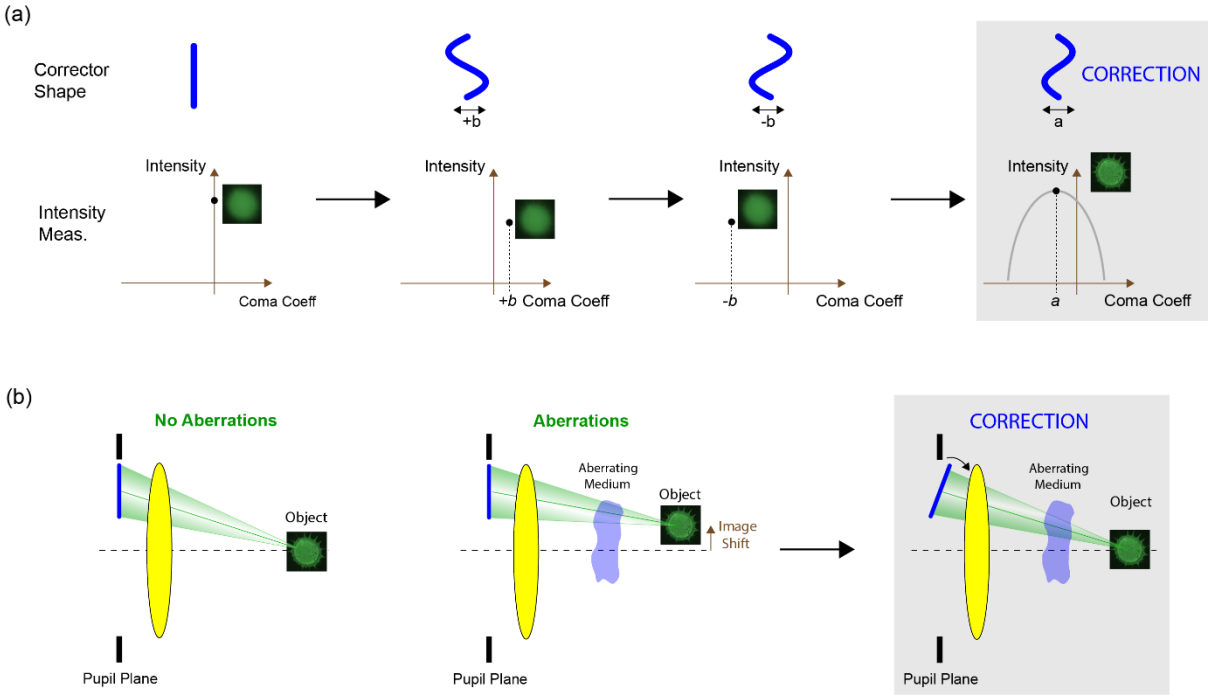

Figure 4. Indirect sensing schemes. (a) In modal AO schemes, different modes, i.e. shapes, are sequentially applied to the corrector. If an aberration, coma in this case, is present, the maximum intensity will occur when the coma applied by the corrector has an equal but opposite magnitude to that introduced by the aberrating medium. Using three intensity measurements; one with the corrector introducing a plane wavefront, and one each with the corrector introducing coma with a chosen magnitude of $-b$ and $+b$, the required correction can be determined using a parabolic fit to the data. (b) In zonal schemes, each zone is modulated. An example of the zonal-based pupil segmentation method is shown in which the required tip and tilt of each segment is determined from shifts in the image. The object is an image of a pollen grain. For simplicity only a single zone is shown but note that the blur in the image results from the image being shifted by different amounts by different zones due to the aberrations.

[H2] Aberration Correctors

Devices that correct wavefront aberrations work by changing the optical path length, which in turn modulates the wavefront phase. There are three main types of correctors as shown in Figure 5. Deformable mirrors consist of a reflective surface that is either continuous (as shown in Figure 5) or segmented. For a continuous surface mirror, when each area of the surface is pulled or pushed, a particular smooth shape known as an influence function **[G]** is created. The surface shape is the sum of these influence functions. Continuous surface deformable mirrors are the most commonly employed corrector across fields. For a segmented device, each mirror facet can either change piston (move forwards or backwards), or changes piston, tip and tilt[16]. Deformable mirrors flatten the wavefront using differences in physical distance travelled by the wave. LCSLMs use differences in refractive index to alter the optical path length; they can be constructed in reflective or transmissive designs[73]. Care must be taken when using LCSLMs as they require the use of (quasi-) monochromatic polarised light **[G]** because the device affects wavelengths differently and is designed for use with linear polarised light. In cases where multiple wavelengths require correction, for example in some fluorescence systems, a deformable mirror may be more appropriate as it does not suffer from chromatic effects. Deformable phase plates are fluidic devices that can change their shape based upon movement of the fluid owing to localised pressure[74,75]. Current designs have far fewer actuators or pixels in comparison to deformable mirrors and LCSLMs, respectively, however they are an attractive option owing to their ability to be easily integrated into and existing imaging system owing to their size and the fact that they are transmissive.

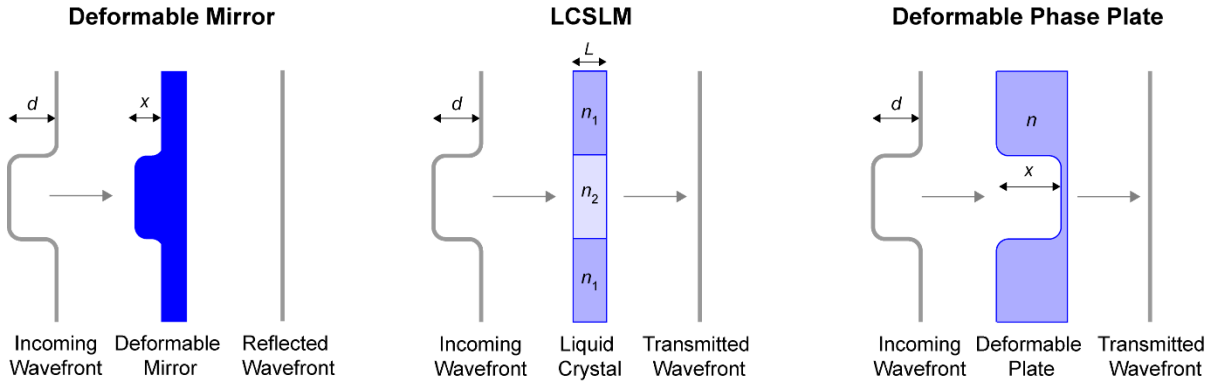

Figure 5. Three main types of corrector. (a) Deformable mirrors consist of a reflective surface that may be continuous or segmented. (b) LCSLMs consist of pixels that are able to change their refractive index, *n*. They can be transmissive or reflective. (c) Deformable phase plates are fluidic devices that are able to change their shape.

When selecting the most suitable corrector for your application, it is important to consider the properties of the aberrations that one will encounter. An important consideration is the maximum peak-to-valley of the wavefront that the device can correct. For a deformable mirror for example, this value is dictated by the stroke **[G]**, which is physical distance that an adaptive element surface can move. The maximum peak-to-valley of the wavefront that can be corrected by a deformable mirror is twice the stroke as the additional path length is imparted to both the incident and reflected light. For vision science for example, as discussed in section 2.2, the required peak-to-valley correction is around 11 μm. Note that for segmented correctors, such as LCSLMs, phase wrapping **[G]** is typically used to increase the effective modulation range. Another consideration is the number of actuators, or pixels in the case of a LCSLM. This depends upon the number of Zernike aberrations that will be corrected. In astronomy for example, where a significant number of Zernike aberrations are corrected, a deformable mirror with thousands of actuators may be required. Note that when considering segmented devices versus continuous surface devices, the number of required actuators can change significantly for the same aberrations[76]. This is related to how well a device can match the incoming wavefront. For relatively smooth wavefronts for example, segmented devices require many more actuators. When correcting for aberrations that change rapidly with time, as is the case for ophthalmology and astronomy, the temporal response of a corrector is another factor to consider. Typically, for the aberrations of the eye, most correctors are faster than the fluctuations that need to be corrected[47]. Astronomical AO systems must run fast enough to keep up with the bulk flow of turbulence, driven by wind above the observatory. System update rates of 1000 Hz or faster may be required[77] for best performance on bright stars. Deformable mirrors are generally faster than LCSLMs and deformable phase plates and so are more suitable as a corrector in this case. There are also secondary factors that affect corrector suitability such as cost, physical size, transmissivity/reflectivity, stability and linearity. Several of the aforementioned factors relates not just to the corrector but to how the corrector interfaces with other parts of the AO system. This interfacing, termed control, is the topic of the next section.

[H2] Control

We discuss here some of the most important factors in calibration and control of an AO system. The main focus is on the control of continuous surface correctors using direct sensing. Note that zonal and modal wavefront control using indirect sensing is presented in Figure 4 and so is not discussed in this section.

[H3] Calibration

Before operating a corrector, it is important to determine the relationship between the control signal, such as voltage, applied to each actuator and the measured wavefront. This relationship is called the influence function. An example influence function for the central actuator of 37-element transmissive phase plate[24] is shown in Figure 6a. The calibration procedure measures these influence functions. The corrector and sensor can be assumed to be a linear system, whereby the overall effect of the corrector on the wavefront is linear superposition of these influence functions. It is also assumed that the sensor is linear in response.

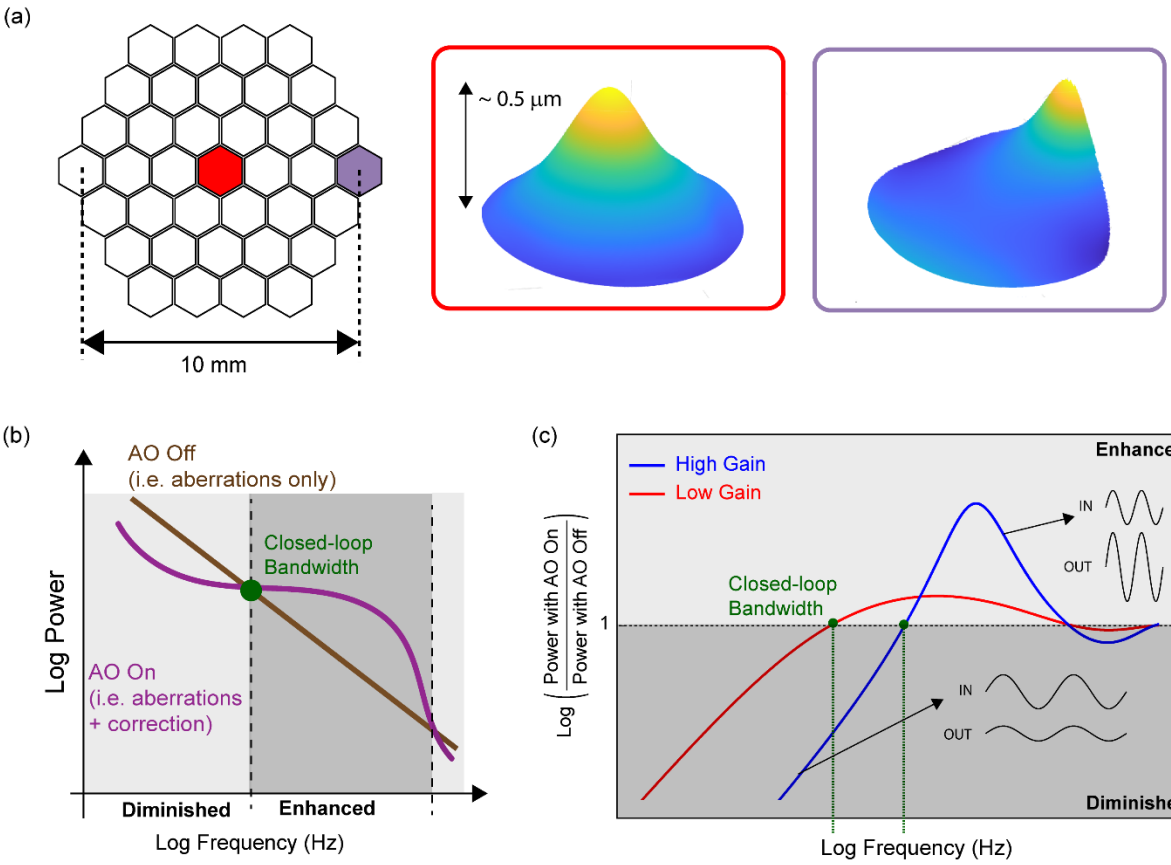

Figure 6. (a) Actuator layout and two example influence functions for a 37-element transmissive phase plate[24]. (b) Typical power spectrum of the fluctuations in the aberrations (rms wavefront error) of the eye or atmospheric turbulence with the AO off, i.e. no correction, and with AO on. (c) The ratio of the power spectra for two gains. The closed-loop bandwidth is the maximum frequency at which the magnitude of the aberration fluctuations can be reduced. Beyond this frequency, the amplitude of the aberration fluctuations are magnified. A higher gain results in a higher closed-loop bandwidth. Although the magnitude of a larger range of frequencies can be reduced, the higher temporal frequencies are enhanced more significantly. The curves are referred to as power rejection curves.

[H3] Implementation

From the calibration procedure, we now have:

$$\boldsymbol{A_{Meas}} = (\boldsymbol{IF})\boldsymbol{C} \quad (3)$$

where $\boldsymbol{A_{Meas}}$ represents a vector of aberration measurements, ***IF*** is the matrix containing the influence functions and ***C*** is a vector of control signals. $\boldsymbol{A_{Meas}}$ can be slopes, modal coefficients, or any other measurement provided that ***IF*** is defined appropriately, i.e. the influence functions are defined as slopes, modal coefficients or any other measurement. The control signals to be sent to the corrective device to generate a given wavefront can be found from:

$$\boldsymbol{C} = (\boldsymbol{IF}^{+})\boldsymbol{A_{Meas}} \quad (4)$$

where $\boldsymbol{IF}^{+}$ is the pseudo-inverse of the matrix containing the influence functions. $\boldsymbol{IF}^{+}$ is referred to as the control matrix and is often calculated using a mathematical technique for matrix inversion referred to as singular value decomposition (SVD)[16]. The control matrix is also referred to as the reconstructor because multiplication of this matrix by $\boldsymbol{A_{Meas}}$ reconstructs the required control values. It is referred to as direct slope or modal reconstructor if the slopes or aberration coefficients are used, respectively. The advantage of SVD is that it allows the calculation of the inverse to be optimised by removing components in its formation that can lead to instability of the system or other problems such as actuator saturation, although other methods are also available[75]. Note that from Equation 4, the required voltages to implement a given aberration mode, for the example of implementing an indirect sensing modal control scheme, can be calculated.

Consider the general AO system shown in Figure 1d. Before the light reaches the sensor, it first passes via the deformable mirror. Consequently, what the sensor sees is the sum of the wavefront due to the aberrations present and the wavefront imparted by the corrector. This is referred to as a closed-loop system and is how the vast majority of AO systems are

operated. If the location of the sensor is such that the light that reaches it does not pass via the corrector, it is referred to as an open-loop system. A major advantage of closed-loop systems is that, in effect, the sensor checks that the wavefront imparted by the corrective device is correct. This is very important as assumptions of linearity between the signal sent to the corrector and the wavefront imparted, as assumed during calibration, do not need to hold exactly true. Closed-loop sensor-based AO systems are typically controlled using a so-called integral controller, although other controllers can be used[16]. The integral controller is implemented as:

$$\boldsymbol{C_{t0+\Delta t}} = \boldsymbol{C_t} - g(\boldsymbol{IF}^{+})\boldsymbol{A_t} \quad (5)$$

where $\boldsymbol{C_t}$ are the control signals at a time *t*, $\boldsymbol{A_t}$ are the aberrations measured at a time *t*, and $\boldsymbol{C_{t0+\Delta t}}$ are the new control signals to be implemented. The gain *g* is a value between zero and one that controls the temporal response and concurrently the stability of the correction. This value has an effect on the temporal frequencies that can be mitigated. This is particularly important for astronomy and vision science where the aberrations vary rapidly over short time scales, as the correction needs to keep up with the changes in the aberrations. As discussed in section 2.2, the magnitude of the aberration dynamics, which can be characterised by the variations in the rms wavefront error, of the eye and atmosphere typically follow an inverse frequency power law as shown schematically in Figure 6b[16,47]. Also shown is the residual power of the fluctuations with dynamic correction of the aberrations. The ratio of these two plots is shown in Figure 6c and referred to as the power rejection curve.

AO systems measure and correct temporally fluctuating aberrations up to a maximum frequency (cut-off) that defines their closed-loop bandwidth **[G]**. This means that aberrations below the cut-off are reduced by the AO (improved image quality) while aberrations above the cut-off are amplified (degrades image quality). The closed-loop bandwidth is affected by many AO parameters. As an example, increasing the control gain, *g*, increases the closed-loop bandwidth but at the expense of increasingly amplifying aberration fluctuations at frequencies above this value (compare red and blue traces in Figure 6d). Thus, an optimal trade-off is sought between the two, which is often determined using both empirical results and predictions from theory. Note that in order to correct for aberration fluctuations up to a given region defined by the closed-loop bandwidth, the aberrations must be measured, and the corrector updated, at significantly faster rates than this frequency limit. For example, to achieve good correction, astronomical AO systems therefore require updates at around 1 kHz or more.

[H1] Results

The different applications of imaging AO have reached different levels of maturity. AO is routinely incorporated into new ground-based telescopes and upgrades. These are usually one-off systems that are dedicated to a particular telescope and given specific names. AO use in vision science and clinical applications continues to increase, driven by the need to elucidate structural and functional changes in the microscopic domain in the intact eye. Like astronomy applications, there is a good understanding of the nature of the aberrations. AO in microscopy is somewhat newer and presents a different challenge, where the range of microscope modalities and specimen types is vast. We outline in this section the AO optical instrumentation advances that have been made in each area. The focus of this section is on what AO can achieve in terms of image enhancement.

[H2] Astronomy

The original proposal for astronomical AO was made in 1953[15]. After a period of development by the military, AO began to be used on astronomical telescopes and is now routinely used on large telescopes around the world. Here we present just a few examples of such systems. For more on the history and development of AO in astronomy see reviews by Beckers[3], Davies and Kasper[7], Rigaut and Neichel[25], and the books by Hardy[26] and Duffner[78].

In astronomical AO, a star (typically called the guide star) is used as the reference for sensing the wavefront. The main source of aberrations to be corrected is atmospheric turbulence, which is blown across the telescope aperture by wind. The output of the wavefront sensor (WFS) is compared to the signal expected for a flat (i.e., no turbulence) wavefront, and the resultant correction is applied to a deformable mirror. The strength of the turbulence and speed of its evolution are not fixed, and AO systems are tuned to maximize correction in current conditions by adjusting the system gain (see Figure 6d).

Among the most well-known and productive general purpose astronomical AO systems are those on the Keck Telescopes. The Keck Telescopes are twin 10 m diameter segmented telescopes on the summit of Mauna Kea, Hawaii, USA. First light for AO on the Keck II telescope occurred on 4 Feb, 1999[79]. This natural guide star (NGS) system was the first on a new generation of 8-10 m telescopes, and delivered Strehl ratios of up to 0.37 in H band (1.6 μm), and demonstrated the dramatic improvements in image quality afforded by AO on large ground-based telescopes. The original Keck AO systems consisted of a separate tip-tilt corrector, a 349 actuator deformable mirror, and a Shack-Hartman WFS[80]. The AO systems on the two telescopes were identical, and in addition to imaging and spectroscopy, AO was used to feed the Keck Interferometer which combined the light from the two telescopes.

Keck AO and the Nasmyth Adaptive Optic System & CONICA instrument (NACOs)[81,82] at ESO's Very Large Telescope (VLT) were instrumental in the study of the Milky Way Galaxy's super-massive black hole, which was the subject of the 2020 Nobel Prize in Physics. We further discuss the contributions of AO to this research in Applications below.

The Keck AO systems were upgraded to use a sodium laser guide star (LGS), which was installed in 2001 and began science operations in 2004 on Keck II[83]. The LGS upgrade significantly improved sky coverage due to no longer requiring a bright natural star in the field. The systems received a wavefront sensor and control upgrade in 2008, which improved the sampling, framerate, and latency[84]. This upgrade delivered further improvements to Strehl ratio and faint star limits for NGS and LGS modes[85].

The latest upgrades to Keck AO are currently in progress. The Keck Planet Imager and Characterize (KPIC[86]) includes an infrared pyramid WFS, as well as a planned 1000 actuator deformable mirror[87]. A key science goal for KPIC is the characterization of exoplanets orbiting late-type stars, for which the IR pyramid WFS will provide significant gains due to such star's higher infrared flux. As the pyramid WFS makes use of light interfered across the entire telescope pupil, rather than smaller sub-apertures, it is more sensitive to low-order aberrations (such as tip and tilt, focus, and astigmatism) than the SH sensor, and takes full advantage of the diffraction limit of large telescopes[88,89]. Another advantage is that it provides for selectable sensitivity and dynamic range. With CCD detectors, on-camera binning lowers the contribution of detector noise, thus allowing higher speeds on fainter stars. As the dynamic range of the can be adjusted by varying the modulation amplitude[60]. Larger amplitudes provide a wider linear range while smaller amplitudes provide more sensitivity and precision. These advantages have led to the adoption of the pyramid WFS in many recent SCAO systems, including the LBT AO systems, SCExAO, and it is under consideration for the upgrade of GPI. Furthermore, each of the coming generation of ELTs will be utilizing pyramid WFS in their AO architectures.

A typical example of a more recently developed astronomical AO system is given by the Magellan AO system (MagAO). The corrector for MagAO is a 585-actuator adaptive secondary mirror (ASM), and the wavefront is sensed by a pyramid WFS (see Figure 3d). ASMs minimize the need for compact optical relays to other DMs, thus minimizing optical losses and minimizing the thermal background noise for infrared imaging, and maximizing the field of view of the imaging system. MagAO is installed on the 6.5 m Magellan Clay telescope[90] at Las Campanas Observatory in Chile. The high number of actuators in the ASM facilitates excellent correction down to visible wavelengths. As shown in Figure 1, spatial resolution depends on wavelength. Working at visible wavelengths thus provides improved spatial resolution, which is demonstrated by MagAO in Figure 7a.

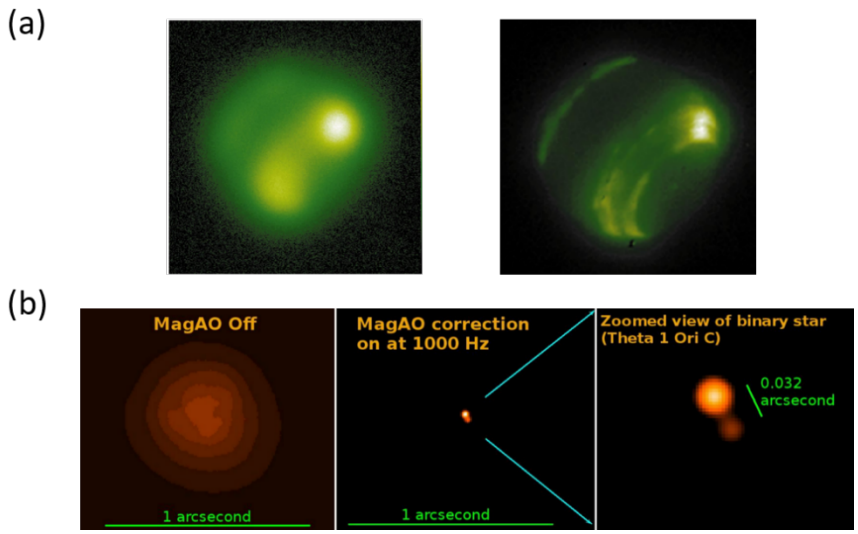

Figure 7. (a) Early Keck AO system demonstration of the benefits of AO for astronomy. Here Neptune is shown in a narrow filter at 1.17 μm showing Methane absorption. The image at left is uncorrected in very good 0.4 arcsec seeing. The image at right is with AO correction. Figure adapted from[79]. (b) Demonstration of high resolution AO in the visible on a 6.5 m telescope with Magellan AO. The star theta-1 Ori C is the brightest star in the Orion Trapezium cluster, a known tight binary. The left panel shows the seeing limited image, with AO off. The middle panel is the same star after closing the AO loop, with the same image field of view. Note the significant concentration of light once diffraction limited performance is achieved. The right panel is zoomed in on the star, demonstrating the spatial resolution of AO on large telescopes. Figure based on[90].

The above results are examples of correction derived from a single guide star in what is called single-conjugate AO (SCAO). SCAO only works well for other objects near that the guide star. The wavefronts from objects farther away, say 10 to 50 seconds of arc depending on wavelength, propagate through slightly different aberrations, and so will suffer from rapidly

degrading correction with distance from the guide star. Multi-conjugate AO (MCAO) can significantly improve the corrected field of view (FOV). MCAO provides good correction over a wide FOV, but imperfectly samples the turbulence above the telescope. Rigaut and Niechel provide an overview of the error sources inherent in MCAO which result in lower Strehl ratio on any single object compared to SCAO[25].

Using multiple guide stars, either natural or artificial stars created with lasers, a wider FOV can be corrected with the Multi-Conjugate Adaptive Optics Demonstrator (MAD) on the 8 m VLT in Chile, shows the power of this technique. Another example of multi-conjugate AO is the Gemini MCAO system (GEMS) on the Gemini South Telescope[91]. GEMS provides uniform sky-coverage of a field as large as 85" by 85", with sky-coverage of 55%.

[H2] Vision Science

It has been known since at least the mid-19th century that the eye contains many aberrations, but methods to effectively measure and correct them did not materialize until the end of the 20th century. These first methods borrowed heavily from the AO ground-based astronomical and military communities. In 1997, the first AO system was used for high-order aberration correction in the eye for both vision improvement and high-resolution retinal imaging[92]. Spurred by this success, AO has been integrated into different types of ophthalmoscopes, principal ones being flood illumination, scanning laser ophthalmoscopy (SLO), and OCT[10,11,93,94]. Because AO is a highly scalable technology, it has been integrated into large laboratory-based ophthalmoscopes, small handheld devices, and systems designed for different species, especially human, monkey and mouse. AO is now routinely used in many scientific and clinical research labs around the world. For more on the history and development of AO for vision science and ophthalmology, see[4,95]. Here we present how AO is applied to the eye and what it can achieve.

The eye's imperfect optics and diffraction caused by the finite size of the eye's pupil (1 to 8 mm diameter) limit the lateral resolution at the retina to a size larger than most retinal cells and cell components; this prevents their visualization. Diffraction can be minimized by dilating the pupil with mydriatic drops, which helps to achieve a resolution of 2–3 microns, sufficient to resolving most major cell types in the retina, including the densely packed cone photoreceptor cells in the fovea. However, this benefit comes at the cost of additional aberrations exposed by dilation. As already described, large population studies have found that the human eye contains significant aberrations, especially for large pupils.

AO increases lateral resolution by a factor of up to five over commercial ophthalmoscopes, permitting resolution of retinal details as small as 2–3 μm and limited only by the effects of diffraction. AO also increases sensitivity as it allows a larger pupil to be used; therefore, more reflected light is captured by the ophthalmoscope (up to a theoretical 20-fold improvement depending on pupil size and scattering properties of the retinal tissue type). This permits more-weakly reflecting retinal structures to be detected.

Figure 8 shows the performance of a representative AO system that was integrated into an optical coherence tomography (OCT) system at Indiana University. As depicted, the AO reduces the wavefront variance of the first seven Zernike orders by two to three orders of magnitude, resulting in diffraction-limited resolution as measured by the wavefront sensor (< λ/14 RMS wavefront error). The second plot in the figure demonstrates that the AO can track and correct temporally fluctuating aberrations up to 4.5 Hz, fast enough for the vast majority of the aberrations in the eye (< 2 Hz)[45,46,96]. Finally, the figure shows the benefit of AO for OCT retinal imaging—revealing thousands of individual cone photoreceptor cells spaced 4.5 μm apart that would otherwise not be seen. A powerful consequence of resolving cells is the ability to track them over time to observe their dynamic behavior. It also allows images to be registered and averaged to increase signal to noise over that of a single image, as illustrated in Figure 8(c) and Supplementary Figure 1.

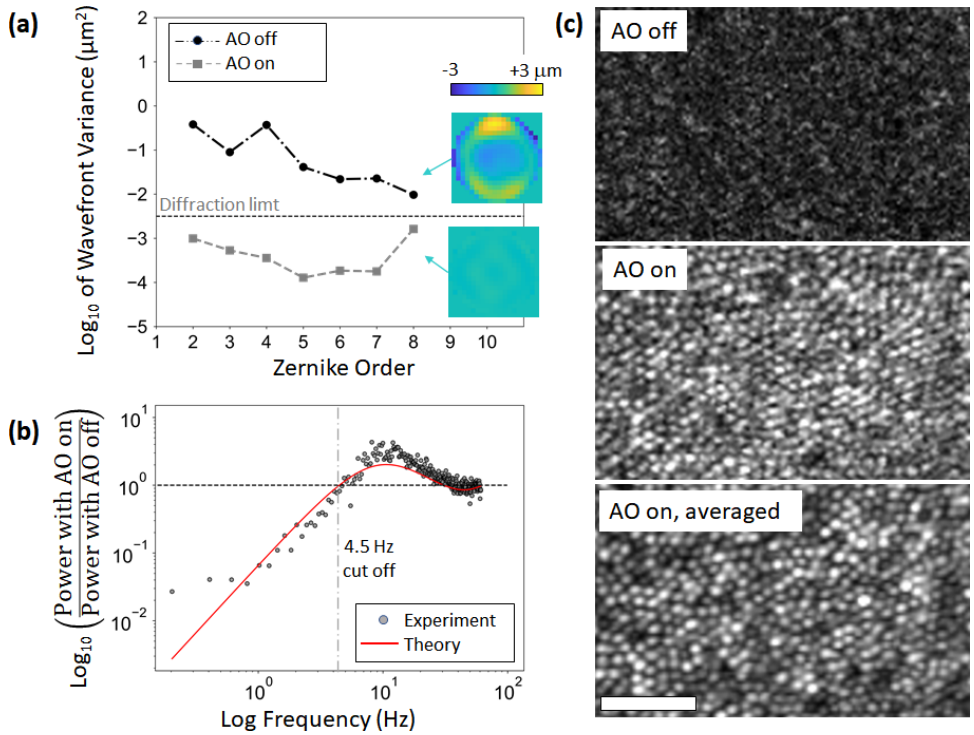

Figure 8. AO performance on a subject with high myopia. The AO system dynamically measured and corrected aberrations over a 6.7 mm pupil at the eye using a 300-lenslet SHWS, a 97-actuator deformable mirror, and a direct-slope reconstructor running at a loop rate of 122 Hz[97]. The measurement and imaging wavelength was 790 nm. The AO is part of the high-resolution AO-OCT imaging system developed at Indiana University[21,98]. A static pre-correction of -6.5 diopters was applied to the deformable mirror to compensate for the subject's spectacle prescription. For loop stability, *g* was set to 0.2 and the 12 SVD mirror modes of highest gain (most unstable) were removed from the control matrix following Section 2.4.2. (a) Spatial performance of the AO was quantified in terms of variance in wavefront height by Zernike order and wavefront aberration map across the eye's pupil (color coded) with AO off and on. (b) Temporal performance of the AO was quantified in terms of the power rejection magnitude following Section 2.4.2. Measurement and theoretical prediction are given. (c) Single and averaged AO-OCT images allow visualization of cone photoreceptor cells at 1 degree from the fovea with AO on, but not off. By registering and averaging images acquired of the same retinal patch, the image signal-to-noise ratio is increased and visualization of cellular structures in the image is improved. Images are cropped from 1° by 1° acquired images. Scale bar is 50 µm. The associated Supplementary Video 1 shows the uncropped patch of cone photoreceptors during image acquisition with AO off and on, and Supplementary Figure 1 shows the full extent of the registered and averaged image.

Over the past two decades, a large number of customized AO systems have been developed in the vision science community. A 2017 survey[99] and a more recent one at the 2019 Center for Adaptive Optics Fall Science Retreat [unpublished data] found that the most common AO platform in today's ophthalmoscopes is a traditional SHWS wavefront sensor and a deformable mirror. This combination is used in Figure 8. In these systems, the SHWS typically samples a large 6.5 mm to 8 mm eye pupil with 300 to 600 lenslets and employs a near-infrared beacon (up to a wavelength of 940 nm) to be less distracting to the subject. While SH sensors dominate today's ophthalmologic AO systems, indirect sensing[51] garners increased interest as it requires no hardware sensor, reducing both cost and system complexity. Numerous types of wavefront correctors (discrete-actuator deformable mirrors, LCSLMs, deformable phase plates, bimorph mirrors, magnetic membrane mirrors, microelectromechanical systems (MEMS) mirrors, and combinations of these corrector types) have been tested on the eye, revealing the need for high-stroke, high-actuator-count correctors[74,76]. The most commonly used corrector today is a ±50-µm-stroke, 97-actuator voice-coil deformable mirror (DM97, ALPAO, France). The combination of a large actuator stroke and count is unique to this corrector. The ±50-µm stroke is nearly ideal, allowing correction of the refractive error in most subjects, thereby precluding the need for auxiliary lenses to correct for the subject's spectacle prescription. The dense pattern of 97 actuators is well matched to the aberration content of the eye, delivering sharp images. However, AO does not perform well on all subjects. More challenging subjects include those with high refractive errors, unclear or highly aberrated optics due to pathology or surgery (e.g., dry eye, keratoconus, cataract, keratoplasty, refractive surgery), elevated eye motion (strabismus), and reduced fixation.

Unlike astronomical AO, the ratio of lenslets to actuators of AO systems for vision science is typically high (3:1 to 6:1). Oversampling with lenslets (high lenslet-to-actuator ratio) is beneficial in that it makes the measurements more robust to pupil edge effects, eye motion, system noise, and drying of the tear film and other local inhomogeneities in the ocular media that can occur with aging. Many ophthalmologic AO systems use zonal control of the corrector via a direct-slope

reconstructor, which has been shown to be more effective than modal control[100]. This is followed by a separate modal reconstructor for Zernike coefficients for real-time AO diagnostics during retinal image acquisition (survey at 2019 Center for Adaptive Optics Fall Science Retreat). Most laboratories develop their own AO control software or partner with laboratories that do. Open-source[101] and commercial software[102,103] are also available, but limited.

Commercialization of AO instruments for the eye is ongoing[104–106], but scientific and clinical discoveries being made with them continue to grow exponentially.

[H3] Microscopy

Adaptive optics was first extended to the field of microscopy around the year 2000. The first implementation of specimen-induced aberration compensation was in a laser scanning fluorescence confocal microscope using an indirect sensing method[107]. Since then, various AO schemes have been developed for a wide range of high-resolution microscopes[1,2] and super-resolution fluorescence methods[108] for applications ranging from neuroscience to cell biology. While AO is becoming more widespread in the research environment, it has not yet been widely adopted in the commercial sphere.

Two types of optical fields are typically involved in microscopy – the illumination light and the emission light, both of which can become aberrated during the imaging process. Depending on the modality of the microscope, the aberrations on the wavefront of one or both optical fields need to be corrected (Supplementary Figure 2). Most widefield microscopy, where emitted light propagates through the sample and forms an image on a camera (Supplementary Figure 2a), requires aberrations to be removed from the detection path. In contrast, two-photon fluorescence microscopy, a point-scanning modality, focuses the excitation light field and collects (but does not image) emitted photons (Supplementary Figure 2b)[109]. To ensure the tightest focus, which leads to highest resolution, signal, and contrast, aberrations of the excitation wavefront need to be removed.

The performance of some microscopy methods depends on both the excitation and emission PSFs. For example, a widefield microscopy method, lattice light sheet microscopy[110], uses structured light to illuminate a single plane and image the fluorescence from this plane on a camera. Confocal microscopy scans a focused excitation laser spot across a sample and detects the emission light that passes through a pinhole, which blocks emission originating from outside the focus; its PSF is equivalent to the product of the excitation and detection PSFs. As a result, diffraction-limited focusing of both the excitation and emission light is required for optimal performance. For these methods, aberrations need to be removed from both the excitation and the emission wavefronts. In the case of lattice light sheet microscopy, because the excitation and emission wavefronts go through different objectives and experience distinct aberrations (Supplementary Fig. 2c), AO corrections have to be carried out for the two wavefronts separately.

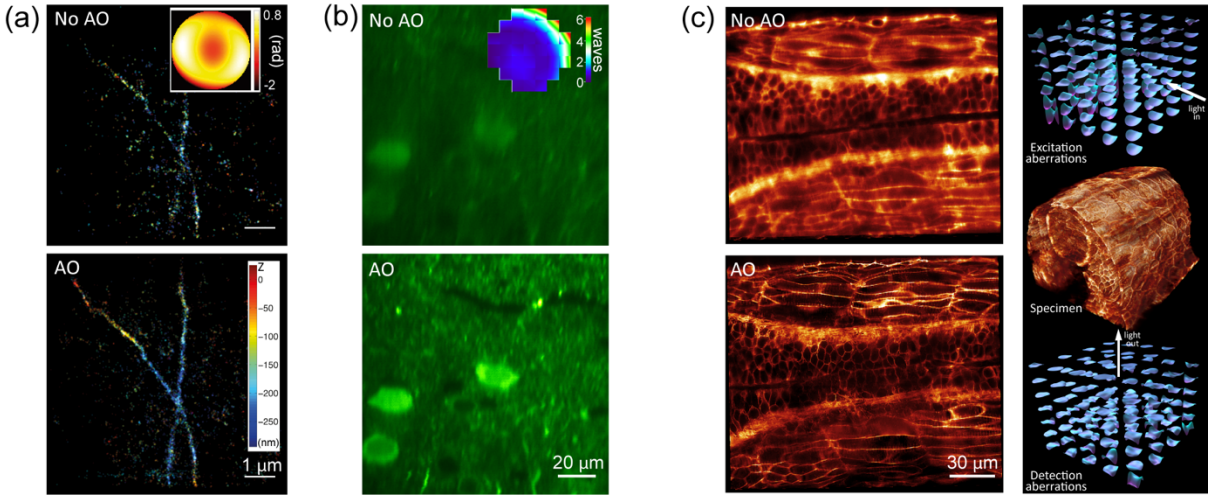

Figure 9. AO in optical microscopy. AO correction on (a) 3D super-resolution widefield microscopy[111], (b) two-photon fluorescence microscopy[29], and (c) lattice light-sheet microscopy[112].

Both the optics in the microscope itself and the samples it investigates can introduce aberrations. The optical system aberration originates from the components of the microscope and does not vary with time. Its presence can be detected from a distorted PSF (usually obtained from the image of a small fluorescent bead) and derived from the PSF using phase retrieval approaches. Optical system aberration should be corrected prior to imaging experiment, so that only sample aberrations may degrade image quality. Sample aberrations arise from the mismatches of the sample refractive index from that of the immersion medium of the microscope objective, which can severely degrade imaging performance, especially for high-resolution microscopy. Super-resolution microscopy, a collection of methods that can achieve resolution beyond the

diffraction limit and reach spatial resolution of tens of nanometres, is even more sensitive to optical aberrations than the diffraction-limited methods, with biological samples a few microns thick capable of substantially reducing image quality.

Sample aberrations may vary spatially, and sometimes also evolve over time (e.g., if imaging a developing embryo)[28,30,112]. Therefore, they need to be measured and corrected in situ. AO has been extensively applied to optical microscopy to remove both system and sample aberrations. Both direct and indirect wavefront sensing methods are used for aberration measurement. For direct wavefront sensing, a Shack-Hartman sensor and a wavefront corrector measure and correct aberrations, respectively, and is applicable throughout transparent samples or to shadow depths of opaque samples; for indirect wavefront sensing, the same corrector is typically employed for both measurement and correction of aberrations, and can be applied to samples with no or substantial light scattering alike. Deformable mirrors, insensitive towards polarization and having broadband high-reflectivity, can efficiently remove aberrations from both illumination and emission wavefronts. For illumination that is monochromatic and polarized, LCSLMs can be applied for wavefront correction to take advantage of their large number of pixels.

By correcting both system and sample-induced aberrations, AO enables optical microscopy to achieve their optimal performance in optically complex samples. Here we list a few examples. In one example[111] (Figure 9a and Supplementary Figure 2d), modal indirect sensing was used to measure the aberration encountered by the fluorescence emission of microtubule structures through a mammalian cell in a widefield super-resolution single molecule localization microscope. A deformable mirror was used as the corrector to remove the cell-induced aberrations from the emitted fluorescence before image formation on a camera, which increased the number of detected fluorescent molecules and improved the measurement accuracy of their positions in 3D.

In another example (Figure 9b and Supplementary Figure 2e), a zonal indirect sensing method was used to measure the tissue-induced aberrations when the excitation light of a two-photon fluorescence microscope travelled through a living mouse brain[29]. A corrective wavefront was then applied to a LCSLM to allow the formation of a diffraction-limited focus *in vivo*, which increased the fluorescence intensity and contrast of neurons in the brain.

Finally, AO was applied to a lattice light-sheet microscope[112] (Fig. 9c and Supplementary Figure 2f), where an 1D lattice of light excited the fluorescence in a thin optical section through one objective and the emitted fluorescence was collected by another objective and imaged on a camera. Direct wavefront sensing with two Shack-Hartman sensors was used to measure the aberrations encountered by both the excitation and emission lights. A LCSLM was used to correct the excitation wavefront whereas a deformable mirror was used to correct the emission wavefront. The high speed of direct wavefront sensing was utilized to measure the excitation and detection aberrations in 140 local volumes. These localized corrections were required to achieve diffraction-limited resolution throughout the image volume within the zebrafish embryo, whose high curvature led to small isoplanatic patches (the FOV over which a single AO correction is valid).

[H1] Applications

We elaborate here on a range of applications where the AO methods describe above have been deployed in order to tackle imaging challenges. The AO methods have enabled imaging advances that provide improved understanding in scientific areas ranging from the role of molecules in biological specimens up to the nature of the cosmos.

[H2] Astronomy

AO is used for Solar astronomy[113], most recently applied at the Daniel K. Inouye Solar Telescope (DKIST)[114]. The earliest use of AO was for observation and tracking of objects orbiting the Earth by the U.S. military[115,116]. Here we review two of the major areas of astronomy and astrophysics impacted by the use of AO, both related to night-time observations.

[H3] The Milky Way Super-Massive Black Hole

AO has made key contribution to the study of the Super-Massive Black Hole (SMBH) at the center of the Milky Way galaxy. The center of the Milky Way was long suspected to harbor a SMBH, expected to coincide with the compact radio source Sgr A * (see Melia and Falcke[117] for a review). It was the use of AO, with the IR WFS on NACO at the VLT[118] and with artificial laser guide stars (LGS) at Keck[119], which allowed the precise measurement of the mass - and its concentration - at the center of the Milky Way and confirmation of its correspondence with Sgr A *. This research led to the 2020 Nobel Prize in Physics being awarded to Andrea Ghez and Reinhard Genzel. Compared to speckle imaging techniques, AO significantly improved the image quality, dynamic range and astrometric precision of such observations (see Figure 10a). Furthermore, AO has enabled spatially resolved spectroscopy[120] with sufficient spectral resolution to measure the radial velocities of individual stars in the nuclear cluster[121,122]. AO continues to make significant contributions to the study of the Milky Way SMBH, for instance see the AO-fed GRAVITY interferometer[123] which measured the gravitational redshift of a star at closest approach to the Milky Way SMBH[124].

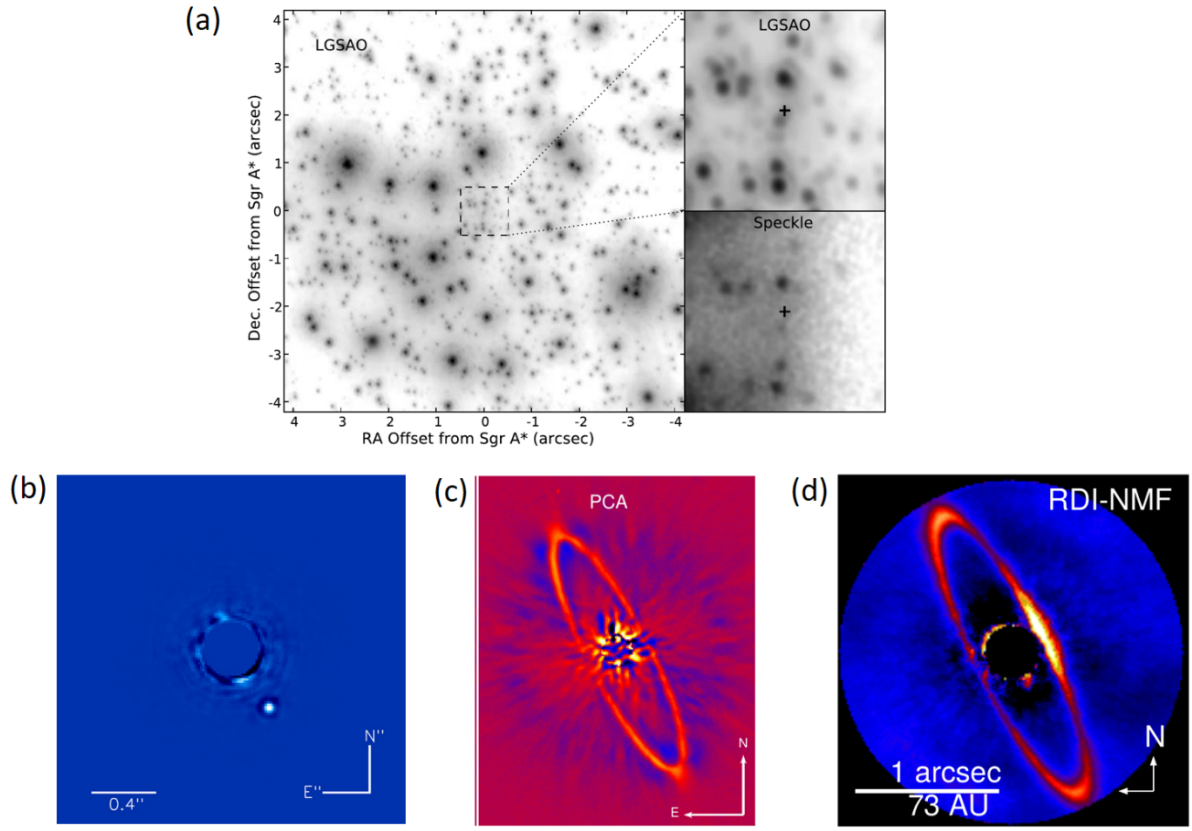

Figure 10: (a) The center of the Milky Way Galaxy, as revealed by laser guide star adaptive optics (LGSAO) on the Keck 10 m telescopes. The right-hand panels compare speckle imaging (bottom) with the remarkable improvement in image quality and sensitivity afforded by LGSAO. The cross marks the location of the supermassive black hole (SMBH) at the galactic center. AO enabled observations such as this have been used to confirm the SMBH, measure its mass, and test general relativity. Figure from[121]. (b) The extrasolar planet beta Pictoris b, as imaged by the Gemini Planet Imager[125]. The HR 4796A debris disk as seen by (c) the SPHERE instrument on VLT[126] and (d) the GPI instrument on Gemini South[127]. These instruments are optimized for high contrast imaging close to bright stars to study exoplanets and circumstellar disks. The well-defined ring of the HR 4796A disk strongly suggests the presence of a planet, though none has yet been detected.

[H3] Extreme AO, Disks, and Extrasolar Planets

One key driver of AO performance has been the study of extrasolar planets and their environments. The first confirmed exoplanet orbiting a main sequence star, detected in the orbital reflex motion of its host star, was announced in 1995[128]. This radial velocity technique and the similarly indirect transit method have accounted for most exoplanet discoveries. By their nature, the radial velocity and transit methods are biased towards close-in planets. The study of more widely separated planets can be accomplished with direct imaging, which requires AO on ground-based telescopes[129]. This radial velocity technique, as well as the similarly indirect transit method, have accounted for a vast majority of exoplanet discoveries. By their nature, the radial velocity and transit methods are biased towards close-in planets. The study of more widely separated planets can be accomplished with direct imaging, which requires AO on ground-based telescopes.

This has led to “extreme” AO (ExAO) instruments, so-called due to the large number of actuators (up to 2000 or more) and high speed (up to 3.6 kHz) needed to image faint objects and structures next to bright stars. Two examples of such systems are the Spectro-Polarimetic High contrast imager for Exoplanets REsearch (SPHERE)[126] and the Gemini Planet Imager (GPI)[125].

The planetary mass object 2M1207b was imaged orbiting a brown dwarf by Chauvin et al[130]. The first images of exoplanets orbiting a main sequence star were obtained by Marois et al[131] observing the star HR 8799. This star is now known to host 4 giant planets[132], with masses of 5-7 Mjup (Mass of Jupiter). Lagrange et al[133,134] imaged a 12.7 Mjup planet orbiting beta Pictoris (Figure 10b), which has been extensively studied with multiple telescopes and AO systems, at wavelengths from 0.9 µm to 5 µm[135–140]. Likewise, the HR 8799 system has been extensively studied[141–146]. These many observations have allowed detailed studies of the planetary atmospheres, and both the HR 8799 planets and beta Pic b show clear orbital motion. Additional examples of well-studied directly imaged planets include HD 95086b[147], HD 106906 b[148], 51 Eri b[149], and PDS 70b[150] and c[151]. For results of recent surveys, see (e.g.)[152] and[153], and see Bowler[129] for a broad review of the field. The study of

circumstellar disks has also benefited from ExAO. Images of the HR 4796A debris disk obtained with SPHERE and GPI are shown in Figure 10c and 10d.

Development of ExAO systems continues. The latest generation of such high-performance exoplanet imaging AO systems include: the Subaru Coronagraphic Extreme AO system (SCExAO)[154], the Magellan Extreme AO system (MagAO-X)[155], and the Keck Planet Imager and Characterizer (KPIC)[86]. Finally, it should be noted that while ExAO seeks to deliver the highest possible Strehl ratio, it has several limitations. The highest performance is only obtainable on bright natural stars, roughly 10th mag and brighter. Such performance cannot be achieved with laser beacons due to the cone effect. Very high actuator count DMs by necessity tend to be small, which limits the field of view of the imaging system. Thus, while ExAO systems are optimized for science cases such as exoplanet imaging and circumstellar disk imaging, general purpose facility AO systems do not need the same capabilities.

[H2] Vision Science

The use of AO makes it possible to study thousands of cells simultaneously in the living retina and to track them longitudinally over days, months, and even years. This unprecedented capability to conduct "living histology" in humans is leading to new discoveries into how the retina and vision function in both healthy and diseased eyes. Furthermore, AO is playing an increasingly important role in how vision science is conducted and how clinicians view and interpret disease in the retina and fundus.

Figure 11 illustrates the breadth of AO use, showing representative images by ophthalmoscope type (AO flood illumination, AO-SLO, and AO-OCT) and specialized sub-methods in healthy and diseased retina. Summarized below and organized by AO ophthalmoscope type is how these images have been used to advance our understanding.

[H3] Flood Illumination

AO flood illumination—an extension of digital flash photography—was the first ophthalmoscope to use AO[92] and the first to be commercialized with it for the clinic (rtx1, Imagine Eyes, France). These systems have been used extensively to image cone photoreceptors: uncovering fundamental optical properties of these cells, classifying for the first time the three cone types in human retina and revealing how disease alters the packing arrangement and other morphological properties of these cells[94,156–159]. The systems have also been extensively used for vascular imaging[94,160,161]. The recent development of transscleral illumination[156] (complementing transpupillary illumination) is expanding the use of AO flood-illumination systems to other cellular structures of the retina.

[H3] Scanning Laser Ophthalmoscopy

AO-SLO — based on raster scanning a focused spot of light across the retina — has been the most extensively used ophthalmoscope for cellular-level based scientific and clinical studies of the retina. Integration of multiply scattered detection[162–166] and single- and multi-photon fluorescence[93,167–176] of intrinsic and extrinsic fluorophores has greatly expanded the structural and functional properties of cells that the AO-SLO can reach. AO-SLO has been used in an enormous number of studies[93,162–182], covering fundamental cell morphology and cell populations, clinical studies of retinal disease, vision restoration, therapeutics, phototoxicity, visual function of cell types, developmental processes, and neurovascular coupling and microvascular perfusion. AO-SLO provides exceptionally detailed images of the retina in both human and animal models.

[H3] Optical Coherence Tomography

AO-OCT—based on low-coherence interferometry and typically raster scanning a focused spot of light across the retina—has been historically a less mature technology than AO flood illumination and AO-SLO. However, in the past few years, it has undergone substantial advances, enabling it to fully utilize its exquisite 3D resolution and sensitivity to study the retina[10,183,184]. State-of-the-art AO-OCT is able to visualize, label free, highly transparent cells and cell components across the entire retinal thickness, permitting reconstruction of a 3D view of the living microscopic retina. Visualizing cells in this way is being used to track structural changes in cells on the scale of nanometers, allowing physiological processes actively occurring in the retina to be reconstructed. Numerous clinical AO-OCT studies are underway to track some of the earliest cellular changes that occur in disease, such as photoreceptors in age-related macular degeneration and retinitis pigmentosa and retinal ganglion cells in glaucoma.

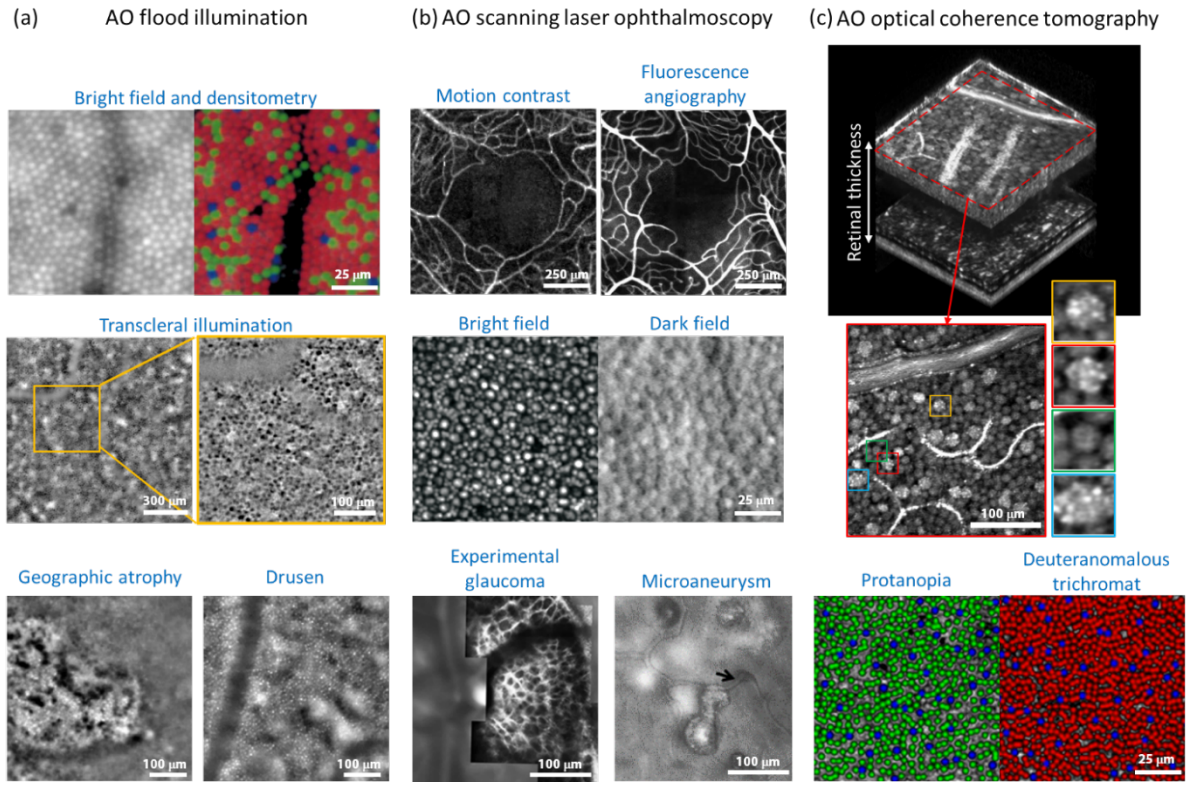

Figure 11. Cellular-level imaging in the living human retina using different AO imaging methods. Examples shown are categorized by ophthalmoscope type: AO flood illumination[156,159], AO-SLO[172,178,185], and AO-OCT[10]. Specialized methods (rows 1 and 2) and disease and color blindness examples (row 3) are labelled under each ophthalmoscope type.

[H2] Microscopy

Without the implementation of AO in microscopy, high-resolution imaging is only practically achievable in thin samples, or in those with optical properties identical with those of the immersion medium of the microscope objective (e.g., air, water, immersion oil). This limits investigation of live biological processes to thin cultured cells or confines structural imaging of fixed samples to those with homogenized refractive index or ultrathin tissue sections. By correcting sample-induced aberrations, AO enables optical microscopy to study biological processes and structures in complex samples at high spatial resolution. Although, so far, the applications of AO to microscopy mostly remain technical, proof-of-principle demonstrations, new biological discoveries have started to emerge.

When applied to cell biology, AO has made it possible to study subcellular processes in 3D over a broad range of length scales in live tissues. Examples include the nanoscale diffusion of clathrin-coated pits (100-nm-sized vesicles used to bring substances inside the cell) in larval zebrafish (Figure 12a)[112], as well as organelle (specialized subunit within a cell with a specific function; e.g., Golgi complex, endoplasmic reticulum, mitochondria) morphology and dynamics during the development of zebrafish embryos (Figure 12b)[112]. The improved spatial resolution by AO enabled the observation of growth cone (subcellular machinery used for cell migration) dynamics in developing spinal cord, immune cell migration in fish ear (Figure 12c), and circulating tumor cells escaping from blood vessels in fish embryos[112]. For super-resolution microscopy, AO has enabled ultrahigh resolution structural imaging of subcellular structures throughout entire mammalian cells (Figure 12d)[186] and complex tissues[187,188]. It has also allowed dynamic super-resolution imaging of subcellular structures in live mouse and zebrafish brains (Figure 12e)[71].

The ability of AO in recovering diffraction-limited PSFs *in vivo* turned out to be essential in the accurate characterization of functional responses of neurons in the living brain[189]. In these applications, microscopy is used in combination with fluorescent sensors that report neuronal activity to determine the external stimuli that neurons and their synapses (junctions between neurons through which information flows) selectively respond to. When imaging synapses hundreds of microns within the mouse brain, a dim, enlarged excitation focus caused by brain-induced aberrations led to reduced fluorescence signal. By exciting structures outside the diffraction-limited focus, an aberrated focus also introduced contamination to the measured functional signal. By increasing the focal electric field strength, AO increased the number of detectable responsive synapses. Furthermore, it reduced the excitation focal volume and effectively removed the contamination (Figure 12f)[28]. As a result, it enabled the discovery of visual orientation-selective inputs from thalamus to the primary visual cortex in the mouse brain[190].

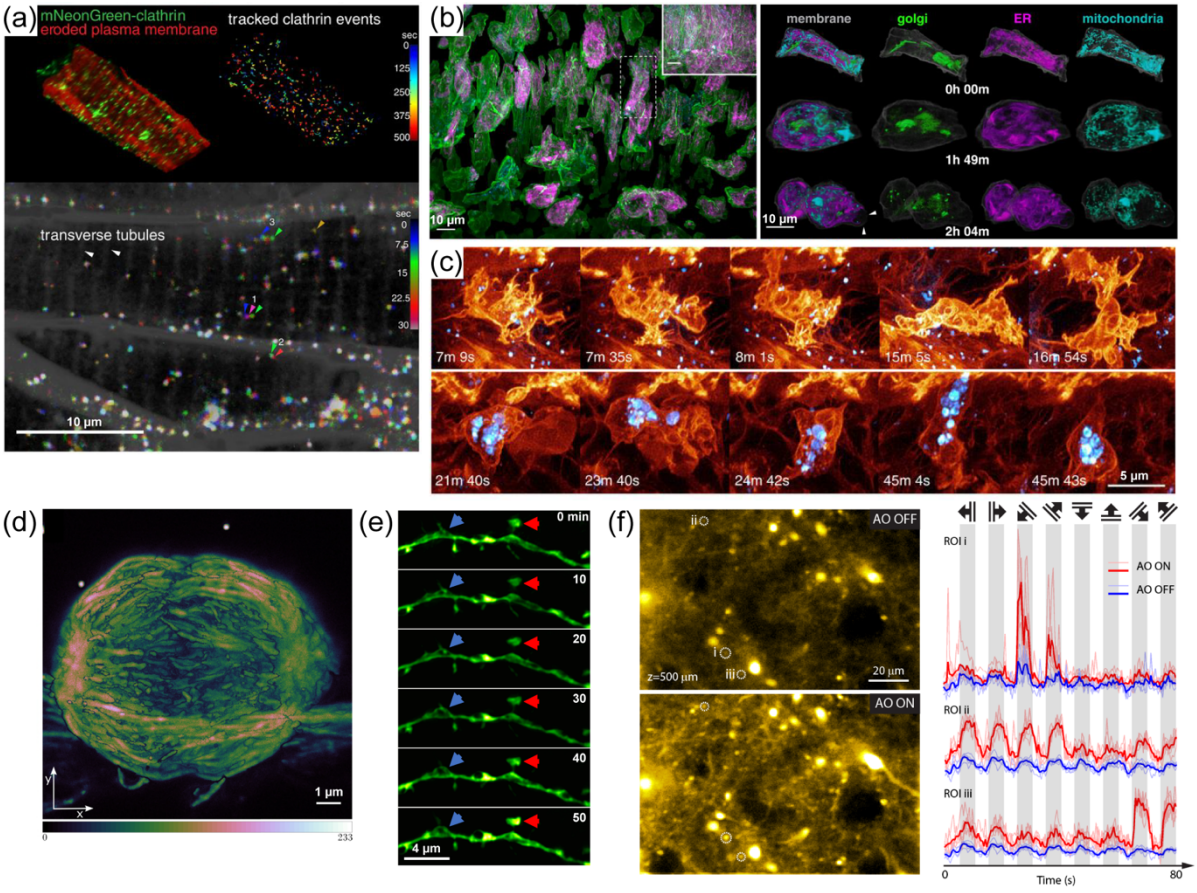

Figure 12. High-resolution optical microscopy with adaptive optics. Lattice light-sheet microscopy of (a) clathrin dynamics[112], organelles morphologies and dynamics[112], and (c) immune cell dynamics[112] in zebrafish embryos. (d) Three-dimensional stimulated emission depletion microscopy of mitotic spindle (projection) in a live cell[186]. (e) *In vivo* structured illumination microscopy images showing structural dynamics of a dendrite at a depth of 25 µm in the brain of a Thy1-GFP line M mouse[71]. (f) left: *In vivo* two-photon fluorescence microscopy to assess the functional calcium response of neurons to visual stimulations (500 µm inside the cortex of a living mouse). Images map the standard deviation of several hundred frames. Right: Calcium transients for the ROIs i-iii as a function of the direction of the grating stimuli (time)[28].

[H1] Reproducibility and data deposition

[H2] Astronomy

Most large observatories maintain publicly accessible data archives. The astronomers who proposed for and were awarded time are typically granted a proprietary period after observations, e.g. 18 months, during which they have exclusive access for analysis and publication. After this period, the data become public and anyone in the world may download it. Such archives include the Gemini Science Archive [https://archive.gemini.edu/searchform], the Keck Observatory Archive [https://www2.keck.hawaii.edu/koa/public/koa.php], the Subaru Telescope Archive System [https://stars2.naoj.hawaii.edu/stars1min.html], and the ESO Science Archive Facility [http://archive.eso.org/cms.html].
AO instruments often provide data reduction tutorials, guides, and software to facilitate user processing of data. Examples include the Keck NIRC2 imager (https://www2.keck.hawaii.edu/inst/nirc2/post_observing.html), SPHERE (http://www.eso.org/sci/software/pipelines/), and GPI (http://docs.planetimager.org/pipeline/).

[H2] Vision Science

Early in the development of AO systems for the eye, it was recognized that a common language was needed to report system performance to facilitate reproducibility. In 2002, the vision science community established a universally accepted naming convention for reporting Zernike coefficients as defined by the OSA ANSI standard[35] (see Figure 3). More recently, many laboratories have converged on a common AO design and integration into the ophthalmoscope (discussed above). Much of the information about these designs are shared: specific hardware, flowcharts and performance specifications of the control software, and schematics of the system optical layout. To reproduce a system requires additional information, namely the actual control software developed and the commercial optical ray tracing design.

The use of a common language and standardized designs have greatly improved the reporting and comparing of performance results. There has been extensive reproducibility of ocular aberration measurements and retinal imaging results across different AO ophthalmoscopes and laboratories. Population studies involving thousands of subjects using Shack-Hartmann aberrometry have been compared and have demonstrated good agreement[44]. Practically every AO ophthalmoscope built has been used to image cone photoreceptors, the density and spacing of which at different locations in the retina are routinely compared to widely accepted measurements obtained in in-vivo imaging[191–193] and histologic[194] studies.

Data deposition of AO technology for vision science continues to be in the peer-reviewed literature. This includes entire textbooks devoted to the topic[4,95] and a recent survey of experts on the state of the field, covering system design, use, and future directions[99]. Data deposition of results with AO instruments is increasing, driven in part by USA federal agency data management and sharing policies. These depositions are more challenging than in astronomy and microscopy as they must follow strict institutional review board rules to protect subject confidentiality.

[H2] Microscopy

The diverse and often live samples investigated by in-house microscopy systems make it difficult to have quantitative comparisons of different AO and microscope modalities. However, the underlying biological principles remain the same. With the increasing application of AO to microscopy, the new biological insights that AO enables will be tested and validated by multiple laboratories. The increasingly widespread requirement of making raw data and custom codes available at online deposits also provides public access to materials beyond those discussed in research papers, which would enable more in-depth analysis and understanding of the published results by general practitioners of optical microscopy. While raw data are often made publicly available through university-specific platforms and custom codes through GitHub, reproducibility in AO microscopy would be improved by a more systematic sharing of control and analysis software. Effective dissemination of know-how is also essential to help make AO more accessible to non-experts who wish to use it in their microscopy applications. Websites collating tutorials and experimental protocols, such as aomicroscopy.org, are particularly enabling for this purpose as they make available a broad range of information at different levels of complexity and details, again not customarily provided by research papers.

[H1] Limitations and optimizations

[H2] Astronomy

There are three main limitations for astronomical AO. The first is the number of controlled degrees of freedom, nominally set by the number of actuators on the corrector, but also the architecture of the WFS and control system. This “fitting error” describes how much turbulence is not corrected.

The second is set by the balance of noise and time-lag. The AO system must run at finite speed due to photon and detector noise. Different WFS architectures have different spatial-frequency dependent response to noise, and WFS detector choice is important for balancing speed vs readout noise. Additionally, readout, computation, and application of correction require finite times. Since turbulence is constantly evolving, the delay between measurement and application causes a correction error. Speed and gain optimization balance the contributions of noise and lag. Further trades can be made with fitting error, both in design and during operation.

The third limitation is the volume of the atmosphere sampled by a given reference. The wavefront from a nearby object propagates through slightly different turbulence, causing a relative error in correction. This “angular anisoplanatism” error limits the well corrected field of view to, depending on wavelength and conditions, on the order of 1” to 30”. This sets the “sky coverage” of AO systems due to the relative rarity of stars bright enough for good correction. This limits the number of targets and science cases for which AO can be used. Anisoplanatism can be mitigated through the use of artificial laser guide stars[83] and using multi-conjugate AO techniques[25]. Other forms of anisoplanatism include “focal anisoplanatism”, or “the cone effect”, from the finite height of an LGS beacon causing only a cone-shaped region of the atmosphere to be sampled; and “tilt anisoplanatism” is due to an offset tip/tilt reference being used during LGS operations, which suffers a different tip/tilt than the target object.

Detailed discussions of these limits can be found in Beckers[3] and Hardy[26].

[H2] Vision Science

The ability of AO to work in a clinical setting remains the most pressing need. Alignment of the eye and AO operation must occur within seconds of the subject placed in the instrument, and AO must work effectively and robustly regardless of subject. Unfortunately, the large variation in eyes and visual performance among individuals make good AO performance challenging. In particular, older eyes and diseased eyes are generally more difficult to image—they have smaller pupils, more frequent drying of the tear film, increased aberrations, eye motion and ocular obstructions (e.g., cataracts), and often have intraocular lenses. The optical properties of the retina also vary, even in healthy subjects, complicating the beacon that

scatters back from the retina and is sensed by AO. Addressing these variations with smarter AO control algorithms that operate more efficiently and reliably will go a long way towards improving clinical use, but these remain a work in progress. Furthermore, best practices of AO control have yet to be established, even at the level of optimal centroiding and handling of SHWS spots.

AO is also limited to the eye's isoplanatic size (~1°), which is much smaller than images acquired with clinical ophthalmoscopes (>20°)[27]. Multi-conjugate AO can increase this size[195,196], but adds significant complexity. AO also produces a narrow depth of focus, which extends over a relatively small fraction of the total retinal thickness. This requires reimaging the same retinal patch multiple times with different focus, thus imposing serious restrictions on imaging studies; no effective solution has been found. Ocular chromatic aberrations[197], light safety[198], and the high cost and complexity of AO technology pose additional challenges for AO ophthalmoscopes. Finally, the benefit of AO is ultimately limited by diffraction caused by the finite size of the eye pupil. Incremental improvements in resolution have been shown using for example sub-Airy disk confocal pinhole detection[199], but substantive improvements will require super resolution methods[200,201].

[H2] Microscopy

The heterogeneity in refractive index, as well as the sometimes high surface curvature, of biological samples can lead to small isoplanatic patch size. Direct wavefront sensing can be achieved at high speed and thus allows region-specific AO corrections to be applied throughout 3D volumes for maximal resolution recovery[30,112]. An alternative approach is multi-conjugate AO, where correctors conjugate to different aberrating layers are used to increase the size of isoplanatic patch, as demonstrated to great effect in astronomy. Methods based on similar principles have been applied to microscopy, where enlargement of isoplanatic patch has been demonstrated in samples with a well-defined, dominant aberrating layer[32,202]. However, because most biological samples introduce aberrations continuously throughout the specimen volume, it remains to be seen whether multi-conjugate AO would lead to much reduced anisoplanatism. For these samples, continued developments in both methodology and wavefront corrector technology are needed, with the ideal correctors having pixels distributed in 3D to match the aberration profile of the sample. Finally, AO methods discussed in this Primer aim to correct aberrations but not scattering. Wavefront shaping has been applied to scattering control in opaque samples – an active research area that has been reviewed recently[203–205].

[H1] Outlook

The future of astronomical AO is apparent in plans for the coming generation of the 25 to 39 m so-called Extremely Large Telescopes (ELTs). These are the 25 m Giant Magellan Telescope (GMT)[206], the Thirty Meter Telescope (TMT)[207], and the European Extremely Large Telescope (E-ELT)[208]. Compared to existing 5-10 m AO equipped observatories, these telescopes will offer ground-breaking improvements in diffraction-limited resolution and sensitivity. The ELTs are each planned to have integrated AO systems, both for high Strehl ratio natural guide star operations and with multiple lasers for wider field corrections and higher sky coverage[209–211].

The widespread adoption of AO for biological imaging (microscopy and vision science) relies on making systems more compact, less expensive, and easier to use. For aberration sensing, compactness is achieved with indirect sensing approaches as they circumvent the need for additional hardware but at the cost of increased interfacing with the image acquisition system. With respect to aberration correction, the most widely used correctors are reflective. Integrating these reflective devices into an existing system, bespoke or commercial, is not trivial, and cannot necessarily be achieved compactly if an additional conjugated plane has to be appended to the original system and if the optical incidence angle on the device has to be optimised to achieve maximal performance. The development of transmissive wavefront shaping devices should make AO systems fully integrable as they can be slotted more simply into imaging systems, without any increase in footprint[75]. Transmissive wavefront shaping devices would be particularly enabling in multiconjugate AO because such devices could potentially be stacked up, which would substantially simplify experimental systems. For now, reflective devices are still preferred because the number of controllable elements is higher and the phase-shift they can impart larger compared to transmissive devices, i.e. reflective devices are better able to shape light for optimal aberration corrections.

In addition to development in hardware, numerical methods will also play an important role in the future of AO technology. The rapidly growing field of artificial intelligence is of particular interest to AO. Substantial effort has recently been dedicated to devising machine learning algorithms capable of evaluating wavefront aberrations. It is anticipated that machine learning will help minimise the number of measurements required for indirect sensing methods without additional instrumentation, thus allowing simplification of the overall system while simultaneously widening its scope of applications. Machine learning for wavefront sensing has been successfully demonstrated in several AO fields using point objects and for retinal imaging[212–215] or for aberration prediction in astronomy[216]. However, significant work remains to be done before machine learning be applied in more complex specimens and implemented in distributable packages for universal usage. One of the main challenges to overcome is the need for large data in the learning step combined with the sensitivity of the outcome on system-specific experimental conditions. While these recent advances are exciting, numerical AO methods are not novel. Indeed, computational AO has been proposed more than 20 years ago for correcting aberrations by mapping the refractive index distribution, modelling the aberrations through ray tracing, and then correcting the effects of the aberrations (using

deconvolution)[217]. While determining the refractive index distribution is not a realisable task on most systems, it has been demonstrated for OCT and the results used to tomographically reconstruct the aberrated wavefront and apply correction using a standard wavefront shaping device or through image post-processing[218]. Phase diversity approaches can also be used in computationally to remove aberrations in fluorescence images[219]. Physical correction is preferred over deconvolution because the additional measurement, the corrected image, yields additional photons, substantially increasing the signal-to-noise ratio and also validating the quality of the corrective process – this fact applies to AO in general and should not be understated.

In this primer, we primarily discussed AO in the context of high-resolution imaging but there are numerous non-imaging applications in which implementing AO has or will yield substantial benefits. Free-space communications is one of them[220]. Similar challenges are encountered in satellite-earth communications as in astronomical imaging because in both contexts the signal has to traverse the atmosphere to reach the Earth's surface. However, the two areas differ in that the source signal can be controlled in space communications, and a beacon embedded to facilitate sensing. Beyond the atmosphere, other turbulent gas and liquid mixtures will have similar dynamic variations in pressure as in the atmosphere, and that includes oceans. AO can therefore be deployed for exploration and communications through oceanic turbulence in a manner analogous to astronomy and space communications[221]. Another non-imaging area of application for AO is laser processing of materials[222]. Laser processing by focusing ultrafast pulses using a high numerical aperture lens is highly susceptible to optical aberrations due to the nonlinearity of the mechanisms at play (e.g. ablation/writing and multiphoton polymerisation). AO is thus key for large scale industrial deployment of the technology. While the implementation of AO for processing has similarities to that in microscopy, the relatively better-known samples (in geometry and optical properties) in laser processing simplify the sensing step and permits taking advantage of wavefront control technology for more advanced applications such as parallel and extend-depth-of-field writing[222]. Another non-imaging field in which AO has been employed is for the optimisation of high-power laser beam control[223]. Finally, a link must be drawn between AO and wavefront control in complex media. The latter aims at compensating the effect of multiple scattering events and therefore will involve the correction of aberrations containing high spatial frequency[205]. In contrast, AO has primarily been concerned with low spatial frequency aberrations. It will be important for future AO and scattering correction technology to bridge this gap and operate across spatial frequency length-scales.

Acknowledgements:

The authors acknowledge support from:
National Institutes of Health grants R01 EY018339 and R01 EY029808 (DM & KK).
National Institutes of Health, U01NS103489 (NJ).
European Research Council 695140 (MJB, KMH, RT)

Conflicts of interest:

D.T.M. and K.K. have a patent on AO-OCT technology. Both authors stand to benefit financially from any commercialization of the technology. N.J. has two patents on AO microscopy technology. MJB holds patents on adaptive optics technology and has a significant interests in the companies Opsydia Ltd. and Aurox Ltd. Otherwise, the authors are not aware of any affiliations, memberships, funding, or financial holdings that might be perceived as affecting the objectivity of this publication.

Glossary

Closed-loop bandwidth

The maximum frequency fluctuation that an adaptive optics system can fully or partially correct.

Collimated

All rays are parallel to each other.

Compensation

Reduction of an effect by modulation of the optical field through the introduction of the *opposite* effect.

Diffraction-limited

There are no aberrations present in the focus. The minimum focal diameter is limited by diffraction due to the wave nature of light.

Dynamic range

The range between the smallest and largest measurable values.

Flood Illumination

A traditional ophthalmoscopy modality based on flash photography in which the image of the illuminated retina is captured by an area detector.

Focal length

The distance between a lens and where the rays meet the optical axis, for incoming collimated light.

Focussed

All rays meet at one point.

Influence function

The shape of modulation produced by a device when a signal is sent to one actuator or pixel.

Lenslets

Miniature lenses usually as part of an array.

Monochromatic polarised light

Light of a single wavelength with a structured oscillation of the electric field.

Noll convention

Mathematical description of aberrated wavefront shapes as proposed by Noll.

Optical fields

An **optical field** describes the distribution of light as an electrical field across space and time in terms of amplitude, phase, frequency, and polarisation.

Optical path length

The **optical path length** is length of the path followed by a light ray multiplied by the refractive index of the medium.

Phase wrapping

Representation of the phase information within the range [0,2π] or [-π, π] radians by adding/subtracting multiples of 2π.

Strehl ratio

The ratio of the intensity of the peak of the aberrated PSF, to that of the diffraction-limited PSF.

Stroke

Maximal physical distance that an adaptive element can move, which limits the optical path length of phase modulation that can be imparted.

Wavelet

A mathematical function basis that is confined in both space and frequency.

References

1. Booth, M. J. Adaptive optical microscopy: the ongoing quest for a perfect image. *Light Sci. Appl.* **3**, e165 (2014).

2. Ji, N. Adaptive optical fluorescence microscopy. *Nat. Methods* **14**, 374–380 (2017).

3. Beckers, J. M. Adaptive Optics for Astronomy: Principles, Performance, and Applications. *Annu. Rev. Astron. Astr.* **31**, 13–62 (1993).

4. Porter, J., Queener, H. M., Lin, J. E., Thorn, K. & Awwal, A. *Adaptive Optics for Vision Science: Principles, Practices, Design and Applications*. (Wiley, 2006).

5. Kubby, J., Gigan, S. & Cui, M. *Adaptive Optical Microscopy for Biological Imaging*. (Cambridge University Press, 2019).

6. Roddier, F. *Adaptive Optics in Astronomy*. (Cambridge University Press, 1999).

7. Davies, R. & Kasper, M. Adaptive Optics for Astronomy. *Annu. Rev. Astron. Astr.* **50**, 305–351 (2012).

8. Ji, N., Sato, T. R. & Betzig, E. Characterization and adaptive optical correction of aberrations during in vivo imaging in the mouse cortex. *Proc. Natl. Acad. Sci. U.S.A.* **109**, 22–27 (2012).

9. Liu, R., Li, Z., Marvin, J. S. & Kleinfeld, D. Direct wavefront sensing enables functional imaging of infragranular axons and spines. *Nat. Methods* **16**, 615–618 (2019).

10. Miller, D. T. & Kurokawa, K. Cellular Scale Imaging of Transparent Retinal Structures and Processes Using Adaptive Optics Optical Coherence Tomography. *Annu. Rev. Vis. Sc.* **6**, 115–148 (2020).

11. Burns, S. A., Elsner, A. E., Sapoznik, K. A., Warner, R. L. & Gast, T. J. Adaptive optics imaging of the human retina. *Prog. Retin. Eye Res.* **68**, 1–30 (2019).

12. Georgiou, M. *et al.* Adaptive optics imaging of inherited retinal diseases. *Brit. J. Ophthalmol.* **102**, 1028 (2018).

13. Roorda, A. & Duncan, J. L. Adaptive Optics Ophthalmoscopy. *Annu. Rev. Vis. Sc.* **1**, 1–32 (2014).

14. Gill, J. S., Moosajee, M. & Dubis, A. M. Cellular imaging of inherited retinal diseases using adaptive optics. *Eye* **33**, 1683–1698 (2019).

15. Babcock, H. W. The Possibility of Compensating Astronomical Seeing. *Publ. Astron. Soc. Pac.* **65**, 229 (1953).

16. Tyson, R. K. *Principles of adaptive optics*. (CRC press, 2015).

17. Vangindertael, J. *et al.* An introduction to optical super-resolution microscopy for the adventurous biologist. *Methods Appl. Fluores.* **6**, 022003 (2018).

18. Dai, Y. *et al.* Active compensation of extrinsic polarization errors using adaptive optics. *Opt. Express* **27**, 35797–35810 (2019).

19. He, C., Hu, Q., Dai, Y. & Booth, M. J. Vectorial adaptive optics - correction of polarization and phase. in *Proc. SPIE 11248, Adaptive Optics and Wavefront Control for Biological Systems VI* 1124808 (2020).

20. Felberer, F., Kroisamer, J.-S., Hitzenberger, C. K. & Pircher, M. Lens based adaptive optics scanning laser ophthalmoscope. *Opt. Express* **20**, 17297–17310 (2012).

21. Liu, Z., Kocaoglu, O. P. & Miller, D. T. In-the-plane design of an off-axis ophthalmic adaptive optics system using toroidal mirrors. *Biomed. Opt. Express* **4**, 3007–3029 (2013).

22. Young, L. K., Morris, T. J., Saunter, C. D. & Smithson, H. E. Compact, modular and in-plane AOSLO for high-resolution retinal imaging. *Biomed. Opt. Express* **9**, 4275–4293 (2018).

23. Thaung, J., Knutsson, P., Popovic, Z. & Owner-Petersen, M. Dual-conjugate adaptive optics for wide-field high-resolution retinal imaging. *Opt. Express* **17**, 4454–4467 (2009).

24. Hampson, K. M. *et al.* Closed-loop multiconjugate adaptive optics for microscopy. in *Proc. SPIE 11248, Adaptive Optics and Wavefront Control for Biological Systems VI* 1124809 (2020).

25. Rigaut, F. & Neichel, B. Multiconjugate Adaptive Optics for Astronomy. *Annu. Rev. Astron. Astr.* **56**, 277–314 (2018).

26. Hardy, J. W. *Adaptive Optics for Astronomical Telescopes*. (Oxford University Press, 1998).

27. Bedggood, P., Daaboul, M., Ashman, R., Smith, G. & Metha, A. Characteristics of the human isoplanatic patch and implications for adaptive optics retinal imaging. *J. Biomed. Opt.* **13**, 024008 (2008).

28. Wang, K. *et al.* Direct wavefront sensing for high-resolution in vivo imaging in scattering tissue. *Nat. Comm.* **6**, 7276 (2015).

29. Wang, C. *et al.* Multiplexed aberration measurement for deep tissue imaging in vivo. *Nat. Methods* **11**, 1037–40 (2014).

30. Wang, K. *et al.* Rapid adaptive optical recovery of optimal resolution over large volumes. *Nat. Methods* **11**, 625–628 (2014).

31. Lin, R., Kipreos, E. T., Zhu, J., Khang, C. H. & Kner, P. Subcellular three-dimensional imaging deep through multicellular thick samples by structured illumination microscopy and adaptive optics. *Nat Commun* **12**, 3148 (2021).

32. Mertz, J., Paudel, H. & Bifano, T. G. Field of view advantage of conjugate adaptive optics in microscopy applications. *Appl. Optics* **54**, 3498–3506 (2015).

33. Lakshminarayanan, V. & Fleck, A. Zernike polynomials: a guide. *J. Mod. Optic.* **58**, 1678–1678 (2011).

34. Noll, R. J. Zernike polynomials and atmospheric turbulence. *J. Opt. Soc. Am.* **66**, 207–210 (1976).

35. Thibos, L. N., Applegate, R. A., Schwiegerling, J. T., Webb, R. & Members, V. S. T. Standards for reporting the optical aberrations of eyes. *J. Refract. Surg.* **18**, S652-60 (2002).

36. Kolmogorov, A. N. Dissipation of energy in the locally isotropic turbulence. *Proc. Royal Soc. Lond. Ser. Math. Phys. Sci.* **434**, 15–17 (1991).

37. Kolmogorov, A. N. The local structure of turbulence in incompressible viscous fluid for very large Reynolds numbers. *Proc. Royal Soc. Lond. Ser. Math. Phys. Sci.* **434**, 9–13 (1991).

38. Thibos, L. N., Hong, X., Bradley, A. & Cheng, X. Statistical variation of aberration structure and image quality in a normal population of healthy eyes. *J. Opt. Soc. Am. A* **19**, 2329 (2002).

39. Devaney, N. *et al.* Correction of ocular and atmospheric wavefronts: a comparison of the performance of various deformable mirrors. *Appl. Optics* **47**, 6550 (2008).

40. Cantalloube, F. *et al.* Wind-driven halo in high-contrast images. *Astron. Astrophys.* **638**, A98 (2020).

41. Males, J. R. & Guyon, O. Ground-based adaptive optics coronagraphic performance under closed-loop predictive control. *J. Astronomical Telesc. Instruments Syst.* **4**, 019001 (2018).

42. Conan, J.-M., Rousset, G. & Madec, P.-Y. Wave-front temporal spectra in high-resolution imaging through turbulence. *J. Opt. Soc. Am. A* **12**, 1559–1570 (1995).

43. Roddier, F., Roddier, D., Northcott, M. J., Graves, J. E. & McKenna, D. L. One-dimensional spectra of turbulence-induced Zernike aberrations: time-delay and isoplanicity error in partial adaptive compensation. *J. Opt. Soc. Am. A* **10**, 957–965 (1993).

44. Salmon, T. O. & Pol, C. van de. Normal-eye Zernike coefficients and root-mean-square wavefront errors. *J. Cataract. Refract. Surg.* **32**, 2064–2074 (2006).

45. Hofer, H., Artal, P., Singer, B., Aragón, J. L. & Williams, D. R. Dynamics of the eye's wave aberration. *J. Opt. Soc. Am. A* **18**, 497 (2001).

46. Diaz-Santana, L., Torti, C., Munro, I., Gasson, P. & Dainty, C. Benefit of higher closed-loop bandwidths in ocular adaptive optics. *Opt. Express* **11**, 2597–2605 (2003).

47. Jarosz, J. *et al.* High temporal resolution aberrometry in a 50-eye population and implications for adaptive optics error budget. *Biomed. Opt. Express* **8**, 2088–2105 (2017).

48. Schmitt, J. M. & Kumar, G. Turbulent nature of refractive-index variations in biological tissue. *Opt. Lett.* **21**, 1310–1312 (1996).

49. Porter, J., Guirao, A., Cox, I. G. & Williams, D. R. Monochromatic aberrations of the human eye in a large population. *J. Opt. Soc. Am. A* **18**, 1793–1803 (2001).

50. Hampson, K., Antonello, J., Lane, R. & Booth, M. Sensorless Adaptive Optics. *Zenodo* (2020) doi:10.5281/zenodo.4066425.

51. Verstraete, H. R. G. W. *et al.* Wavefront sensorless adaptive optics OCT with the DONE algorithm for in vivo human retinal imaging [Invited]. *Biomed. Opt. Express* **8**, 2261–2275 (2017).

52. Shack, R. V. & Platt, B. C. Production and use of a lenticular Hartmann screen. *J. Opt. Soc. Am.* **61**, 656–660 (1971).

53. Thomas, S. *et al.* Comparison of centroid computation algorithms in a Shack–Hartmann sensor. *Mon. Not. R. Astron. Soc.* **371**, 323–336 (2006).

54. Geng, Y. *et al.* Optical properties of the mouse eye. *Biomed. Opt. Express* **2**, 717–738 (2011).

55. Akondi, V. & Dubra, A. Multi-layer Shack-Hartmann wavefront sensing in the point source regime. *Biomed. Opt. Express* **12**, 409–432 (2021).

56. Rahman, S. A. & Booth, M. J. Direct wavefront sensing in adaptive optical microscopy using backscattered light. *Appl. Optics* **52**, 5523–5532 (2013).

57. Poyneer, L. A. Scene-based Shack-Hartmann wave-front sensing: analysis and simulation. *Appl. Optics* **42**, 5807–5815 (2003).

58. Ashida, Y. *et al.* Imaging performance of microscopy adaptive-optics system using scene-based wavefront sensing. *J Biomed Opt* **25**, 123707 (2020).

59. Laslandes, M., Salas, M., Hitzenberger, C. K. & Pircher, M. Influence of wave-front sampling in adaptive optics retinal imaging. *Biomed. Opt. Express* **8**, 1183–1200 (2017).

60. Ragazzoni, R. Pupil plane wavefront sensing with an oscillating prism. *J. Mod. Optic* **43**, 289–293 (1996).

61. Engler, B., Weddell, S. & Clare, R. Wavefront sensing with prisms for astronomical imaging with adaptive optics. *2017 Int Conf Image Vis Comput New Zealand Ivcnz* 1–7 (2017).

62. Chamot, S. R., Dainty, C. & Esposito, S. Adaptive optics for ophthalmic applications using a pyramid wavefront sensor. *Opt. Express* **14**, 518–526 (2006).

63. Iglesias, I. Pyramid phase microscopy. *Opt. Lett.* **36**, 3636–3638 (2011).

64. Berto, P., Rigneault, H. & Guillon, M. Wavefront sensing with a thin diffuser. *Opt. Lett.* **42**, 5117–5120 (2017).

65. Nishizaki, Y. *et al.* Deep learning wavefront sensing. *Opt. Express* **27**, 240–251 (2019).

66. Antonello, J., Barbotin, A., Chong, E. Z., Rittscher, J. & Booth, M. J. Multi-scale sensorless adaptive optics: application to stimulated emission depletion microscopy. *Opt. Express* **28**, 16749–16763 (2020).

67. Facomprez, A., Beaurepaire, E. & Débarre, D. Accuracy of correction in modal sensorless adaptive optics. *Opt. Express* **20**, 2598–2612 (2012).

68. Ji, N., Milkie, D. E. & Betzig, E. Adaptive optics via pupil segmentation for high-resolution imaging in biological tissues. *Nat. Methods* **7**, 141–147 (2009).

69. Milkie, D. E., Betzig, E. & Ji, N. Pupil-segmentation-based adaptive optical microscopy with full-pupil illumination. *Opt. Lett.* **36**, 4206–4208 (2011).

70. Gonsalves, R. A. Phase Retrieval And Diversity In Adaptive Optics. *Opt. Eng.* **21**, 215829 (1982).

71. Turcotte, R. *et al.* Dynamic super-resolution structured illumination imaging in the living brain. *Proc. Natl. Acad. Sci. U.S.A.* **116**, 9586–9591 (2019).

72. Sauvage, J.-F., Fusco, T., Rousset, G. & Petit, C. Calibration and precompensation of noncommon path aberrations for extreme adaptive optics. *J. Opt. Soc. Am. A* **24**, 2334–2346 (2007).

73. Maurer, C., Jesacher, A., Bernet, S. & Ritsch-Marte, M. What spatial light modulators can do for optical microscopy. *Laser Photonics Rev.* **5**, 81–101 (2011).

74. Bonora, S. *et al.* Wavefront correction and high-resolution in vivo OCT imaging with an objective integrated multi-actuator adaptive lens. *Opt. Express* **23**, 21931–21941 (2015).

75. Banerjee, K., Rajaeipour, P., Ataman, Ç. & Zappe, H. Optofluidic adaptive optics. *Appl. Optics* **57**, 6338–6344 (2018).

76. Doble, N., Miller, D. T., Yoon, G. & Williams, D. R. Requirements for discrete actuator and segmented wavefront correctors for aberration compensation in two large populations of human eyes. *Appl. Optics* **46**, 4501–4514 (2007).

77. Guyon, O. Extreme Adaptive Optics. *Annu. Rev. Astron. Astr.* **56**, 315–355 (2018).

78. Duffner, R. W. *The Adaptive Optics Revolution: A History*. (University of New Mexico Press, 2009).

79. Wizinowich, P. *et al.* First Light Adaptive Optics Images from the Keck II Telescope: A New Era of High Angular Resolution Imagery. *Publ. Astron. Soc. Pac.* **112**, 315–319 (2000).

80. Dam, M. A. van, Mignant, D. L. & Macintosh, B. A. Performance of the Keck Observatory adaptive-optics system. *Appl. Optics* **43**, 5458–5467 (2004).

81. Lenzen, R. *et al.* NAOS-CONICA first on sky results in a variety of observing modes. in *Proc. SPIE 4841, Instrument Design and Performance for Optical/Infrared Ground-based Telescopes* 944–952 (2003).

82. Rousset, G. *et al.* NAOS, the first AO system of the VLT: on-sky performance. in *Adaptive Optical System Technologies II* vol. 4839 140–149 (2003).

83. Wizinowich, P. L. *et al.* The W. M. Keck Observatory Laser Guide Star Adaptive Optics System: Overview. *Publ. Astron. Soc. Pac.* **118**, 297–309 (2006).

84. Johansson, E. M. *et al.* Upgrading the Keck AO wavefront controllers. in *Proc. SPIE 7015, Adaptive Optics Systems, 70153E* (2008).

85. Dam, M. A. van *et al.* The W. M. Keck Observatory Laser Guide Star Adaptive Optics System: Performance Characterization. *Publ Astron Soc Pac* **118**, 310–318 (2006).

86. Mawet, D. *et al.* Keck Planet Imager and Characterizer: concept and phased implementation. in *Adaptive Optics Systems V* 99090D (2016).

87. Plantet, C. *et al.* Adaptive optics with an infrared pyramid wavefront sensor at Keck. *J. Astronomical Telesc. Instruments Syst.* **6**, (2020).

88. Ragazzoni, R. & Farinato, J. Sensitivity of a pyramidic Wave Front sensor in closed loop Adaptive Optics. *Astron. Astrophys.* **350**, L23–L26 (1999).

89. Vérinaud, C. On the nature of the measurements provided by a pyramid wave-front sensor. *Opt Commun* **233**, 27–38 (2004).

90. Close, L. M. *et al.* Diffraction-limited Visible Light Images of Orion Trapezium Cluster With the Magellan Adaptive Secondary AO System (MagAO). *Astrophys. J.* **774**, 94 (2013).

91. d'Orgeville, C. *et al.* Gemini South multi-conjugate adaptive optics (GeMS) laser guide star facility on-sky performance results. in *Adaptive Optics Systems III* vol. 84471Q (2012).

92. Liang, J., Williams, D. R. & Miller, D. T. Supernormal vision and high-resolution retinal imaging through adaptive optics. *J. Opt. Soc. Am.* **14**, 2884–2892 (1997).

93. Hunter, J. J., Merigan, W. H. & Schallek, J. B. Imaging Retinal Activity in the Living Eye. *Annu. Rev. Vis. Sc.* **5**, 15–45 (2019).

94. Paques, M. *et al.* Adaptive optics ophthalmoscopy: Application to age-related macular degeneration and vascular diseases. *Prog. Retin. Eye Res.* **66**, 1–16 (2018).

95. Hampson, K. M. *Introduction to Adaptive Optics for Vision Science*. (CRC Press, 2021).

96. Gofas-Salas, E. *et al.* High loop rate adaptive optics flood illumination ophthalmoscope with structured illumination capability. *Appl. Optics* **57**, 5635–5642 (2018).

97. Liu, Y. *et al.* High-speed adaptive optics for imaging the living human eye with optical coherence tomography. in *Invest. Ophthalmol. Vis. Sci.* vol. 61 222 (2020).

98. Kocaoglu, O. P., Turner, T. L., Liu, Z. & Miller, D. T. Adaptive optics optical coherence tomography at 1 MHz. *Biomed. Opt. Express* **5**, 4186–4200 (2014).

99. Marcos, S. *et al.* Vision science and adaptive optics, the state of the field. *Vision Res* **132**, 3–33 (2017).

100. Li, K. Y., Mishra, S., Tiruveedhula, P. & Roorda, A. Comparison of control algorithms for a MEMS-based adaptive optics scanning laser ophthalmoscope. *Am. Control. Conf.* 3848–3853 (2009).

101. Jonnal, R. S. CIAO: Community Inspired Adaptive Optics. *Zenodo* (2020) doi:10.5281/zenodo.3903941.

102. ALPAO Core Engine, ALPAO, France,. https://www.alpao.com/adaptive-optics/ao-softwares.html (2020).

103. WaveTuneTM, Imagine Eyes, France,. https://www.imagine-eyes.com/products/aokit/ (2020).

104. RTX1 Adaptive Optics Retinal Camera, Imagine Eyes, France,. https://www.imagine-eyes.com/products/rtx1/ (2020).

105. The Apaeros™ AOSLO, Boston Micromachines Corporation, USA,. http://bostonmicromachines.com/apaeros-retinal-imaging-system-aoslo/ (2020).

106. Compact Adaptive Optics Retinal Imager, Physical Sciences Inc., USA,. http://www.psicorp.com/products/laser-based-sensors/compact-adaptive-optics-retinal-imager-caori (2020).

107. Booth, M. J., Neil, M. A. A., Juškaitis, R. & Wilson, T. Adaptive aberration correction in a confocal microscope. *Proc. Natl. Acad. Sci. U.S.A.* **99**, 5788–5792 (2002).

108. Booth, M., Andrade, D., Burke, D., Patton, B. & Zurauskas, M. Aberrations and adaptive optics in super-resolution microscopy. *Microscopy* **64**, 251–261 (2015).

109. Denk, W., Strickler, J. & Webb, W. Two-photon laser scanning fluorescence microscopy. *Science* **248**, 73–76 (1990).

110. Chen, B.-C. *et al.* Lattice light-sheet microscopy: imaging molecules to embryos at high spatiotemporal resolution. *Science* **346**, 1257998 (2014).

111. Burke, D., Patton, B., Huang, F., Bewersdorf, J. & Booth, M. J. Adaptive optics correction of specimen-induced aberrations in single-molecule switching microscopy. *Optica* **2**, 177–185 (2015).

112. Liu, T.-L. *et al.* Observing the cell in its native state: Imaging subcellular dynamics in multicellular organisms. *Science* **360**, eaaq1392 (2018).

113. Schmidt, D., Rimmele, T., Marino, J. & Wöger, F. A review of solar adaptive optics. in *Adaptive Optics Systems V, 99090X* (2016).

114. Johnson, L. C. *et al.* First light with adaptive optics: the performance of the DKIST high-order adaptive optics. in *Adaptive Optics Systems VII, 114480T* (2020).

115. Collins, G. P. Making Stars to See Stars: DOD Adaptive Optics Work is Declassified. *Phys. Today* **45**, 17–21 (1992).

116. Fugate, R. Q. The Starfire Optical Range 3.5-m Adaptive Optical Telescope. in *Proc. SPIE 4837, Large Ground-based Telescopes* 934–943 (2003).

117. Melia, F. & Falcke, H. The Supermassive Black Hole at the Galactic Center. *Annu. Rev. Astron. Astr.* **39**, 309–352 (2001).

118. Genzel, R. *et al.* The Stellar Cusp around the Supermassive Black Hole in the Galactic Center. *Astrophys. J.* **594**, 812–832 (2003).

119. Ghez, A. M. *et al.* The First Laser Guide Star Adaptive Optics Observations of the Galactic Center: Sgr A*'s Infrared Color and the Extended Red Emission in its Vicinity. *Astrophys. J.* **635**, 1087–1094 (2005).

120. Gezari, S. *et al.* Adaptive Optics Near-Infrared Spectroscopy of the Sagittarius A* Cluster. *Astrophys. J.* **576**, 790–797 (2002).

121. Ghez, A. M. *et al.* Measuring Distance and Properties of the Milky Way's Central Supermassive Black Hole with Stellar Orbits. *Astrophys. J.* **689**, 1044–1062 (2008).

122. Eisenhauer, F. *et al.* SINFONI in the Galactic Center: Young Stars and Infrared Flares in the Central Light-Month. *Astron. J.* **628**, 246–259 (2005).

123. Collaboration, G. *et al.* First light for GRAVITY: Phase referencing optical interferometry for the Very Large Telescope Interferometer. *Astron. Astrophys.* **602**, A94 (2017).

124. Collaboration, G. *et al.* Detection of the gravitational redshift in the orbit of the star S2 near the Galactic centre massive black hole. *Astron. Astrophys.* **615**, L15 (2018).

125. Macintosh, B. *et al.* First light of the Gemini Planet Imager. *Proc. Natl. Acad. Sci. U.S.A.* **111**, 12661–12666 (2014).

126. Beuzit, J.-L. *et al.* SPHERE: the exoplanet imager for the Very Large Telescope. *Astron Astrophys* **631**, A155 (2019).

127. Chen, C. *et al.* Multiband GPI Imaging of the HR 4796A Debris Disk. *Astrophys. J.* **898**, 55 (2020).

128. Mayor, M. & Queloz, D. A Jupiter-mass companion to a solar-type star. *Nature* **378**, 355–359 (1995).

129. Bowler, B. P. Imaging Extrasolar Giant Planets. *Publ. Astron. Soc. Pac.* **128**, 102001 (2016).

130. Chauvin, G. *et al.* A giant planet candidate near a young brown dwarf: Direct VLT/NACO observations using IR wavefront sensing. *Astron. Astrophys.* **425**, L29–L32 (2004).

131. Marois, C. *et al.* Direct Imaging of Multiple Planets Orbiting the Star HR 8799. *Science* **322**, 1348–1352 (2008).

132. Marois, C., Zuckerman, B., Konopacky, Q. M., Macintosh, B. & Barman, T. Images of a fourth planet orbiting HR 8799. *Nature* **468**, 1080–1083 (2010).

133. Lagrange, A.-M. *et al.* A probable giant planet imaged in the β Pictoris disk: VLT/NaCo deep L'-band imaging. *Astron. Astrophys.* **493**, L21–L25 (2008).

134. Lagrange, A.-M. *et al.* A giant planet imaged in the disk of the young star beta Pictoris. *Science* **329**, 57–59 (2010).

135. Bonnefoy, M. *et al.* High angular resolution detection of β Pictoris b at 2.18 µm. *Astron. Astrophys.* **528**, L15 (2011).

136. Males, J. R. *et al.* Magellan adaptive optics first-light observations of the exoplanet β pic b. I. direct imaging in the far-red optical with MagAO+ VisAO and in the near-ir with nici. *Astrophys. J.* **786**, 32 (2014).

137. Baudino, J.-L. *et al.* Interpreting the photometry and spectroscopy of directly imaged planets: a new atmospheric model applied to β Pictoris b and SPHERE observations. *Astron. Astrophys.* **582**, A83 (2015).

138. Morzinski, K. M. *et al.* Magellan Adaptive Optics first-light observations of the exoplanet beta Pic b. II. 3-5 micron direct imaging with MagAO+Clio, and the empirical bolometric luminosity of a self-luminous giant planet. *Astrophys. J.* **815**, 108 (2015).

139. Chilcote, J. *et al.* 1–2.4µm Near-IR Spectrum of the Giant Planet β Pictoris b Obtained with the Gemini Planet Imager. *Astrophys. J.* **153**, 182 (2017).

140. Nielsen, E. L. *et al.* The Gemini Planet Imager Exoplanet Survey: Dynamical Mass of the Exoplanet β Pictoris b from Combined Direct Imaging and Astrometry. *Astrophys. J.* **159**, 71 (2020).

141. Bowler, B. P., Liu, M. C., Dupuy, T. J. & Cushing, M. C. Near-infrared Spectroscopy of the Extrasolar Planet HR 8799 b. *Astrophys. J.* **723**, 850 (2010).

142. Currie, T. *et al.* A combined Subaru/VLT/MMT 1-5 µm study of planets orbiting HR 8799: Implications for atmospheric properties, masses, and formation. *Astrophys. J.* **729**, 128 (2011).

143. Ingraham, P. *et al.* Gemini Planet Imager Spectroscopy of the HR 8799 planets c and d. *Astrophys. J.* **794**, L15 (2014).

144. Skemer, A. J. *et al.* Directly imaged LT transition exoplanets in the mid-infrared. *Astrophys. J.* **792**, 17 (2014).

145. Barman, T. S., Konopacky, Q. M., Macintosh, B. & Marois, C. Simultaneous detection of water, methane, and carbon monoxide in the atmosphere of exoplanet hr 8799 b. *Astrophys. J.* **804**, 61 (2015).

146. Wang, J. J. *et al.* Dynamical constraints on the HR 8799 planets with GPI. *Astrophys. J.* **156**, 192 (2018).

147. Rameau, J. *et al.* Discovery of a probable 4-5 Jupiter-mass exoplanet to HD 95086 by direct-imaging. *Astrophys. J. Lett.* **772**, L15 (2013).

148. Bailey, V. *et al.* HD 106906 b: A planetary-mass companion outside a massive debris disk. *Astrophys. J.* **780**, L4 (2013).

149. Macintosh, B. *et al.* Discovery and spectroscopy of the young jovian planet 51 Eri b with the Gemini Planet Imager. *Science* **350**, 64–67 (2015).

150. Keppler, M. *et al.* Discovery of a planetary-mass companion within the gap of the transition disk around PDS 70. *Astron. Astrophys.* **617**, A44 (2018).

151. Haffert, S. Y. *et al.* Two accreting protoplanets around the young star PDS 70. *Nat. Astronomy* **3**, 749–754 (2019).

152. Stone, J. M. *et al.* The LEECH Exoplanet Imaging Survey: Limits on Planet Occurrence Rates under Conservative Assumptions. *Astrophys. J.* **156**, 286 (2018).

153. Nielsen, E. L. *et al.* The Gemini Planet Imager Exoplanet Survey: Giant Planet and Brown Dwarf Demographics from 10 to 100 au. *Astrophys. J.* **158**, 13 (2019).

154. Jovanovic, N. *et al.* The Subaru Coronagraphic Extreme Adaptive Optics System: Enabling High-Contrast Imaging on Solar-System Scales. *Publ Astron Soc Pac* **127**, 890–910 (2015).

155. Males, J. R. *et al.* MagAO-X: project status and first laboratory results. **10703**, 9 (2018).

156. Laforest, T. *et al.* Transscleral optical phase imaging of the human retina. *Nat. Photonics* **14**, 439–445 (2020).

157. Bedggood, P. & Metha, A. Mapping flow velocity in the human retinal capillary network with pixel intensity cross correlation. *Plos One* **14**, e0218918 (2019).

158. Bek, T. Fine structure in diabetic retinopathy lesions as observed by adaptive optics imaging. A qualitative study. *Acta Ophthalmol.* **92**, 753–758 (2014).

159. Roorda, A. & Williams, D. R. The arrangement of the three cone classes in the living human eye. *Nature* **397**, 520–522 (1999).

160. Bedggood, P. & Metha, A. Direct visualization and characterization of erythrocyte flow in human retinal capillaries. *Biomed. Opt. Express* **3**, 3264–3277 (2012).

161. Rha, J. *et al.* Adaptive optics flood-illumination camera for high speed retinal imaging. *Opt. Express* **14**, 4552–4569 (2006).

162. Rossi, E. A. *et al.* Imaging individual neurons in the retinal ganglion cell layer of the living eye. *Proc. Natl. Acad. Sci. U.S.A.* **114**, 586–591 (2017).

163. Burns, S. A. *et al.* In vivo adaptive optics microvascular imaging in diabetic patients without clinically severe diabetic retinopathy. *Biomed. Opt. Express* **5**, 961–974 (2014).

164. Guevara-Torres, A., Joseph, A. & Schallek, J. B. Label free measurement of retinal blood cell flux, velocity, hematocrit and capillary width in the living mouse eye. *Biomed. Opt. Express* **7**, 4228–4249 (2016).

165. Guevara-Torres, A., Williams, D. R. & Schallek, J. B. Imaging translucent cell bodies in the living mouse retina without contrast agents. *Biomed. Opt. Express* **6**, 2106–2119 (2015).

166. Scoles, D., Sulai, Y. N. & Dubra, A. In vivo dark-field imaging of the retinal pigment epithelium cell mosaic. *Biomed. Opt. Express* **4**, 1710–23 (2013).

167. Qin, Z. *et al.* Adaptive optics two-photon microscopy enables near-diffraction-limited and functional retinal imaging in vivo. *Light Sci. Appl.* **9**, 79 (2020).

168. Cua, M. *et al.* Coherence-Gated Sensorless Adaptive Optics Multiphoton Retinal Imaging. *Sci. Rep.* **6**, 32223 (2016).

169. Sharma, R., Williams, D. R., Palczewska, G., Palczewski, K. & Hunter, J. J. Two-Photon Autofluorescence Imaging Reveals Cellular Structures Throughout the Retina of the Living Primate Eye. *Invest. Ophth. Vis. Sci.* **57**, 632–46 (2016).

170. Yin, L. *et al.* Imaging light responses of retinal ganglion cells in the living mouse eye. *J. Neurophysiol.* **109**, 2415–2421 (2013).

171. Yin, L. *et al.* Imaging light responses of foveal ganglion cells in the living macaque eye. *J. Neurosci.* **34**, 6596–6605 (2014).

172. Mo, S. *et al.* Imaging Foveal Microvasculature: Optical Coherence Tomography Angiography Versus Adaptive Optics Scanning Light Ophthalmoscope Fluorescein Angiography. *Invest. Ophth. Vis. Sci.* **57**, OCT130–OCT40 (2016).

173. Zawadzki, R. J. *et al.* Adaptive-optics SLO imaging combined with widefield OCT and SLO enables precise 3D localization of fluorescent cells in the mouse retina. *Biomed. Opt. Express* **6**, 2191–2210 (2015).

174. Jung, H., Liu, T., Liu, J., Huryn, L. A. & Tam, J. Combining multimodal adaptive optics imaging and angiography improves visualization of human eyes with cellular-level resolution. *Commun. Biology* **1**, 189 (2018).

175. Morgan, J. I. W., Dubra, A., Wolfe, R., Merigan, W. H. & Williams, D. R. In Vivo Autofluorescence Imaging of the Human and Macaque Retinal Pigment Epithelial Cell Mosaic. *Invest. Ophth. Vis. Sci.* **50**, 1350 (2009).

176. Rossi, E. A. *et al.* In vivo imaging of retinal pigment epithelium cells in age related macular degeneration. *Biomed. Opt. Express* **4**, 2527–2539 (2013).

177. Xu, X. *et al.* Retinal Pigment Epithelium Degeneration Associated With Subretinal Drusenoid Deposits in Age-Related Macular Degeneration. *Am. J. Ophthalmol.* **175**, 87–98 (2017).

178. Cunefare, D. *et al.* RAC-CNN: multimodal deep learning based automatic detection and classification of rod and cone photoreceptors in adaptive optics scanning light ophthalmoscope images. *Biomed. Opt. Express* **10**, 3815–3832 (2019).

179. Takayama, K. *et al.* High-resolution imaging of the retinal nerve fiber layer in normal eyes using adaptive optics scanning laser ophthalmoscopy. *Plos One* **7**, e33158 (2012).

180. Huang, G. *et al.* Imaging Glaucomatous Damage Across the Temporal Raphe. *Invest. Ophth. Vis. Sci.* **56**, 3496–504 (2015).

181. Tam, J., Tiruveedhula, P. & Roorda, A. Characterization of single-file flow through human retinal parafoveal capillaries using an adaptive optics scanning laser ophthalmoscope. *Biomed. Opt. Express* **2**, 781–793 (2011).

182. Ivers, K. M. *et al.* In Vivo Changes in Lamina Cribrosa Microarchitecture and Optic Nerve Head Structure in Early Experimental Glaucoma. *Plos One* **10**, e0134223 (2015).

183. Jonnal, R. S. *et al.* A Review of Adaptive Optics Optical Coherence Tomography: Technical Advances, Scientific Applications, and the Future. *Invest. Ophth. Vis. Sci.* **57**, OCT51–OCT68 (2016).

184. Pircher, M. & Zawadzki, R. J. Review of adaptive optics OCT (AO-OCT): principles and applications for retinal imaging [Invited]. *Biomed. Opt. Express* **8**, 2536–2562 (2017).

185. Tam, J. *et al.* Disruption of the Retinal Parafoveal Capillary Network in Type 2 Diabetes before the Onset of Diabetic Retinopathy. *Invest. Ophth. Vis. Sci.* **52**, 9257–9266 (2011).

186. Zdankowski, P., McGloin, D. & Swedlow, J. R. Full volume super-resolution imaging of thick mitotic spindle using 3D AO STED microscope. *Biomed. Opt. Express* **10**, 1999–2009 (2019).

187. Patton, B. R. *et al.* Three-dimensional STED microscopy of aberrating tissue using dual adaptive optics. *Opt. Express* **24**, 8862 (2016).

188. Huang, F. *et al.* Ultra-High Resolution 3D Imaging of Whole Cells. *Cell* **166**, 1028–1040 (2016).

189. Turcotte, R., Liang, Y. & Ji, N. Adaptive optical versus spherical aberration corrections for in vivo brain imaging. *Biomed. Opt. Express* **8**, 3891–3902 (2017).

190. Sun, W., Tan, Z., Mensh, B. D. & Ji, N. Thalamus provides layer 4 of primary visual cortex with orientation- and direction-tuned inputs. *Nat. Neurosci.* **19**, 308–315 (2015).

191. Li, K. Y., Tiruveedhula, P. & Roorda, A. Intersubject Variability of Foveal Cone Photoreceptor Density in Relation to Eye Length. *Invest. Ophth. Vis. Sci.* **51**, 6858–6867 (2010).

192. Song, H., Chui, T. Y. P., Zhong, Z., Elsner, A. E. & Burns, S. A. Variation of Cone Photoreceptor Packing Density with Retinal Eccentricity and Age. *Invest. Ophth. Vis. Sci.* **52**, 7376–7384 (2011).

193. Wang, Y. *et al.* Human foveal cone photoreceptor topography and its dependence on eye length. *Elife* **8**, e47148 (2019).

194. Curcio, C. A., Sloan, K. R., Kalina, R. E. & Hendrickson, A. E. Human photoreceptor topography. *J. Comp. Neurol.* **292**, 497–523 (1990).

195. Bedggood, P. A., Ashman, R., Smith, G. & Metha, A. B. Multiconjugate adaptive optics applied to an anatomically accurate human eye model. *Opt. Express* **14**, 8019–8030 (2006).

196. Laslandes, M., Salas, M., Hitzenberger, C. K. & Pircher, M. Increasing the field of view of adaptive optics scanning laser ophthalmoscopy. *Biomed. Opt. Express* **8**, 4811–4826 (2017).

197. Zawadzki, R. J. *et al.* Ultrahigh-resolution optical coherence tomography with monochromatic and chromatic aberration correction. *Opt. Express* **16**, 8126–8143 (2008).

198. *American National Standard for Safe Use of Lasers*. (Laser Institute of America, 2014).

199. Sredar, N., Fagbemi, O. E. & Dubra, A. Sub-Airy Confocal Adaptive Optics Scanning Ophthalmoscopy. *Transl. Vis. Sci. Technology* **7**, 17 (2018).

200. Shroff, S. A., Fienup, J. R. & Williams, D. R. Phase-shift estimation in sinusoidally illuminated images for lateral superresolution. *J. Opt. Soc. Am. A* **26**, 413–424 (2009).

201. DuBose, T. B., LaRocca, F., Farsiu, S. & Izatt, J. A. Super-resolution retinal imaging using optically reassigned scanning laser ophthalmoscopy. *Nat. Photonics* **13**, 257–262 (2019).

202. Paudel, H. P., Taranto, J., Mertz, J. & Bifano, T. Axial range of conjugate adaptive optics in two-photon microscopy. *Opt. Express* **23**, 20849–20857 (2015).

203. Horstmeyer, R., Ruan, H. & Yang, C. Guidestar-assisted wavefront-shaping methods for focusing light into biological tissue. *Nat. Photonics* **9**, 563–571 (2015).

204. Mosk, A. P., Lagendijk, A., Lerosey, G. & Fink, M. Controlling waves in space and time for imaging and focusing in complex media. *Nat. Photonics* **6**, 283–292 (2012).

205. Yoon, S. *et al.* Deep optical imaging within complex scattering media. *Nat. Rev. Phys.* **2**, 141–158 (2020).

206. McCarthy, P. J. *et al.* Overview and status of the Giant Magellan Telescope project. in *Proc. SPIE 10700, Ground-based and Airborne Telescopes VII, 1070012* (2018).

207. Skidmore, W., Anupama, G. C. & Srianand, R. The Thirty Meter Telescope International Observatory facilitating transformative astrophysical science. *Curr. Sci.* **113**, 639–648 (2017).

208. Marchiori, G., Rampini, F., Ghedin, L. & Bressan, R. ELT design status: the most powerful ground telescope. in *Proc. SPIE 10700, Ground-based and Airborne Telescopes VII, 1070021* (2018).

209. Vernet, E. *et al.* Adaptive optics at the ESO ELT. in *Proc. SPIE 10703, Adaptive Optics Systems VI, 1070310* (2018).

210. Crane, J. *et al.* NFIRAOS adaptive optics for the Thirty Meter Telescope. in *Proc. SPIE 10703, Adaptive Optics Systems VI, 107033V* (2018).

211. Bouchez, A. H. *et al.* An overview and status of GMT active and adaptive optics. in *Proc. SPIE 10703, Adaptive Optics Systems VI, 107030W* (2018).

212. Cunefare, D. *et al.* Deep learning based detection of cone photoreceptors with multimodal adaptive optics scanning light ophthalmoscope images of achromatopsia. *Biomed. Opt. Express* **9**, 3740–3756 (2018).

213. Kyono, T. *et al.* Machine learning for quality assessment of ground-based optical images of satellites. *Opt. Eng.* **59**, 051403 (2020).

214. Cumming, B. P. & Gu, M. Direct determination of aberration functions in microscopy by an artificial neural network. *Opt. Express* **28**, 14511–14521 (2020).

215. Saha, D. *et al.* Practical sensorless aberration estimation for 3D microscopy with deep learning. *Opt. Express* **28**, 29044 (2020).

216. Andersen, T., Owner-Petersen, M. & Enmark, A. Image-based wavefront sensing for astronomy using neural networks. *J. Astron. Telesc. Instrum. Syst* **6**, 1 (2020).

217. Kam, Z., Hanser, B., Gustafsson, M. G. L., Agard, D. A. & Sedat, J. W. Computational adaptive optics for live three-dimensional biological imaging. *Proc. Natl. Acad. Sci. U.S.A.* **98**, 3790–3795 (2001).

218. Iyer, R. R., Liu, Y.-Z. & Boppart, S. A. Automated sensorless single-shot closed-loop adaptive optics microscopy with feedback from computational adaptive optics. *Opt. Express* **27**, 12998–13014 (2019).

219. Kner, P. Phase diversity for three-dimensional imaging. *J Opt Soc Am* **30**, 1980 (2013).

220. Tyson, R. K. Adaptive optics and ground-to-space laser communications. *Appl. Optics* **35**, 3640–3646 (1996).

221. Chang, H. *et al.* Performance analysis of adaptive optics with a phase retrieval algorithm in orbital-angular-momentum-based oceanic turbulence links. *Appl. Optics* **58**, 6085–6090 (2019).

222. Salter, P. S. & Booth, M. J. Adaptive optics in laser processing. *Light Sci. Appl.* **8**, 110 (2019).

223. Lubeigt, W., Grol, P. van, Valentine, G. & Burns, D. Use of Intracavity Adaptive Optics in Solid-State Lasers Operation at 1 µm. in *Adaptive Optics for Industry and Medicine* 217–227 (2005).